
Decomposing the Generalization Gap in PROTAC Activity Prediction: Variance Attribution and the Inter-Laboratory Ceiling

Thor Klamt^{1,*}  Wolfgang Nejdil^{1,2}  Ming Tang^{1,2} 

¹L3S Research Center, Leibniz Universität Hannover, Appelstraße 9a, 30167 Hannover, Germany

²Institute of Data Science (Knowledge-Based Systems),
Faculty of Electrical Engineering and Computer Science,
Leibniz Universität Hannover, Appelstraße 9a, 30167 Hannover, Germany

*thor.klamt@gmail.com

Abstract

Machine-learning predictors of biochemical activity often exhibit large random-split-to-leave-one-target-out generalisation gaps that have been documented but not decomposed. We frame this as an evaluation-science question and use targeted protein degradation as the empirical test bed. PROTACs (proteolysis-targeting chimeras) are heterobifunctional small molecules that induce targeted protein degradation, with more than forty candidates currently in clinical trials; published predictors of PROTAC activity report AUROC values of 0.85 to 0.91 under random-split cross-validation, while the leave-one-target-out (LOTO) protocol of Ribes et al. reduces performance to approximately 0.67. Random-split cross-validation rewards within-target interpolation, whereas LOTO measures the novel-target prediction that de-novo design depends on. We decompose this gap and identify inter-laboratory measurement variance as the dominant component, anchored by a within-target cross-laboratory cascade that bounds the inter-laboratory contribution at 0.124 AUROC, substantially above the 0.05 contribution from binarisation-threshold choice across four labelling schemes. Across eight published architectures and ESM-2 protein language models scaled to 3B parameters, LOTO AUROC plateaus near 0.67 under the canonical evaluation protocol, with a comparable plateau under SMILES-level deduplication of the training partition; a 21-dimensional, 2000-trial hyperparameter optimisation across head architectures, molecular encoders, and protein encoders cannot break this ceiling, and the rank-1 single-seed configuration regresses by 0.161 AUROC under multi-seed validation, matching a closed-form selection-bias prediction [Bailey et al., 2014, Bailey and López de Prado, 2014]. Few-shot $k=5$ stratified per-target retraining combined with ADMET features lifts 65-target LOTO AUROC from 0.668 to 0.7050, and post-hoc Platt scaling recovers raw output to within the 0.05 well-calibrated threshold. We release PROTAC-Bench, a curated benchmark of 10,748 PROTAC degradation measurements across 173 targets and 65 LOTO folds, alongside the variance-decomposition framework, the per-target calibration protocol, and the evaluation code, providing a methodological template for variance attributions in other small-data therapeutic settings.

1 Introduction

PROTACs are heterobifunctional small molecules that bind a target protein and an E3 ubiquitin ligase to induce the target’s polyubiquitination and proteasomal degradation. By eliminating the target rather than inhibiting its catalytic function, this mechanism in principle expands the druggable landscape to scaffold proteins, transcription factors, and other classes that lack the active-site geometry classical small-molecule inhibitors require, with more than forty PROTAC candidates currently in clinical trials

and a medicinal-chemistry pipeline that depends on activity predictors for compound-library triage. Published PROTAC predictors Li et al. [2022], Liu et al. [2025], Chen et al. [2025] report AUROCs of 0.85 to 0.91 under random-split cross-validation. Ribes et al. [2024] show that approximately 80 percent of random-split test entries share their UniProt target with a training entry, and that the leave-one-target-out (LOTO) protocol drops macro performance to approximately 0.67 against a matched random-CV macro of 0.755 and pooled 0.902. The pooled-to-macro aggregation thus separates from cross-target generalisation, with the latter dominated by cross-laboratory variance (Section 5). The gap is not in dispute. What remains unanswered is whether it reflects models that cannot extrapolate to novel targets, or measurement variance that no binary-label predictor can resolve. Under the second, the gap reflects inter-laboratory measurement noise and labelling heterogeneity rather than learning failure, with cross-domain precedent in molecular-property and pair-input prediction Graber et al. [2025], Pahikkala et al. [2015]. Our analysis identifies inter-laboratory measurement variance as the dominant component, with the reproducibility floor as the operational ceiling at current dataset scale; the 65 LOTO-eligible targets reflect a deliberate trade-off in favour of within-target measurement density and multi-publication replicate structure over corpus size (Section 3.1).

We report four contributions: (i) a variance-decomposition framework with three convergent ceiling estimates at 0.668 to 0.678 AUROC; (ii) an architecture-invariant performance plateau across eight published predictors and ESM-2 protein language models scaled to 3 billion parameters, with the rank-1 of 2,000 hyperparameter-optimisation trials regressing by 0.161 AUROC under multi-seed validation in agreement with the Bailey-López de Prado closed-form selection-bias prediction Bailey et al. [2014], Bailey and López de Prado [2014], Cawley and Talbot [2010]; (iii) a per-target recovery analysis where few-shot $k=5$ stratified retraining lifts 65-target LOTO AUROC from 0.668 to 0.7050, and a four-factor factorial decomposition that collapses an apparent +0.042 AUROC warhead-transfer effect to within seed noise once few-shot calibration is included as a co-factor; and (iv) PROTAC-Bench (10,748 measurements across 173 targets, 65 LOTO folds), evaluation code, Croissant metadata with MLCommons RAI extension, and a reusable dual-LLM metadata-enrichment pipeline.

2 Related Work

PROTAC and targeted-degrader machine learning. Computational PROTAC activity prediction has been approached through deep architectures combining target-pocket encoders with PROTAC molecular encoders. DeepPROTACs Li et al. [2022] introduced a pocket graph convolutional network coupled to a BiLSTM over PROTAC fragment SMILES (0.847 random-split AUROC); DegradeMaster Liu et al. [2025] extended this with an equivariant graph neural network over the ternary complex (approximately 0.94 random-split AUROC under supervised setting per their Table 2); PROTAC-STAN Chen et al. [2025] introduced ternary-attention over Morgan fingerprints, ESM-650M target embeddings, and an E3-ligase one-hot vector (0.883 random-split). Per-architecture replication notes appear in Appendices F and O. Ribes et al. [2024] are the only prior authors to evaluate under LOTO, reporting an AUROC drop to 0.604; the random-CV-to-LOTO gap was documented but not decomposed. Generative approaches address PROTAC design rather than activity prediction Guan et al. [2023], Li et al. [2024, 2023] and assume a reliable activity oracle that the present work shows is currently unavailable. Ternary-complex structure prediction has advanced rapidly Dunlop et al. [2025], Riepenhausen et al. [2026], Passaro et al. [2025], Xue et al. [2025]; the structural approaches evaluated here predate AlphaFold-3 PROTAC accessibility, and Section 4.3 demonstrates that structure-prediction quality under currently-evaluable tools does not translate to activity-prediction performance under held-out-target evaluation.¹

Cold-split evaluation protocols. Distinguishing random-split from cold-split evaluation has cross-domain precedent. Park and Marcotte [2012] introduced the C1, C2, C3, and C4 evaluation classes for protein-protein interaction prediction, formalised by Pahikkala et al. [2015] for drug-target interaction prediction (PROTAC-Bench’s LOTO protocol corresponds to the C3 setting), and Bennett et al. [2024] demonstrated that current sequence-based PPI predictors collapse to chance under leakage-free evaluation. Cold-split evaluation under scaffold or similarity-controlled protocols reveals performance degradation that random splits hide Liu et al. [2024], Steshin [2023], Ektefaie et al. [2024], Arevalo et al. [2024]; the continuous similarity-resolution sweep in Appendix C integrates this framing with the binary LOTO protocol. Tossou et al. [2024] report up to 60 percent performance degradation under real-world molecular OOD; Joeres et al. [2025] introduce DataSAIL for principled

¹Concurrent published predictors and benchmarks not included in the canonical-evaluation sweep (AiPROTAC, DeepPROTACs 2.0, DeepPSA, Protap Yan et al. [2025]) require pipeline-specific reimplementations outside the canonical scope and are deferred to future work.

split construction with quantitative leakage scoring; Roberts et al. [2017] established block cross-validation for ecological models in the presence of spatial autocorrelation, the ecological analogue of inter-laboratory measurement variance.

Methodological lineage. The decomposition in Section 5 extends a methodological lineage of attributing apparent generalisation gaps to measurement-variance components: Cronbach generalizability theory [Cronbach, 1972], pharmacogenomic and cross-source IC50 variance [Haibe-Kains et al., 2013, Landrum and Riniker, 2024], train-test redundancy in molecular-property benchmarks [Graber et al., 2025], hyperparameter-optimisation selection bias [Cawley and Talbot, 2010, Bailey et al., 2014, Bailey and López de Prado, 2014, Bouthillier et al., 2021], the transportability framework where LOTO is an explicit S-node intervention [Pearl and Bareinboim, 2014], architecture-invariance under cold-split evaluation [Xia et al., 2023, Deng et al., 2023, Gulrajani and Lopez-Paz, 2020], accidental-taxonomy and shortcut-learning interpretations of inverted PLM scaling [Hallee et al., 2025, Cheng et al., 2024, Geirhos et al., 2020, Kumar et al., 2022], simple-baseline outperformance of parameterised meta-learning [Tian et al., 2020, Chen et al., 2019, Stanley et al., 2021], selective-classification inversion under dataset shift [Jones et al., 2020, Ovadia et al., 2019], and broader generalizability concerns [Yarkoni, 2022, D’Amour et al., 2022]. The present work contributes four methodological moves anchored to this lineage: variance-share decomposition of the cold-split gap, the Bailey-López de Prado closed-form selection-bias anchor applied to ML hyperparameter regression, within-target multi-publication replicate structure as a benchmark feature, and Platt scaling recovery under cold-target distributional shift.

3 PROTAC-Bench

3.1 Dataset

PROTAC-Bench is constructed from the publicly available PROTAC-DB 3.0 Ge et al. [2025], the curated benchmark of Ribes et al. [2024], and DegradeMaster Liu et al. [2025], merged into 10,748 entries spanning 173 unique UniProt protein targets, with within-target measurement density and inter-laboratory replicate structure prioritised over corpus size since the variance attribution that anchors the analysis (Section 5) requires per-target depth that catalogue-style compendia at larger compound counts cannot support. Each entry is associated with a SMILES representation of the PROTAC molecule, the target UniProt identifier, the recruited E3 ligase (CRBN, VHL, or other), continuous DC50 and Dmax measurements where available, and a binarised activity label following the convention of prior work Ribes et al. [2024]: active if DC50 below 1 μ M OR Dmax above 50 percent. The release CSV carries binary activity labels; continuous DC₅₀ and D_{max} values are pointed to upstream PROTAC-DB 3.0 Ge et al. [2025] where source-traceable, with user-side recovery supported by the released compound-target identifier mapping. The activity rate across the full benchmark is 0.658. The LOTO-cohort positive rate of 0.672 produces a random-baseline AUPRC equal to the prior (versus AUROC’s random-baseline of 0.500); AUPRC absolute values fall within ± 0.02 of AUROC across architectures, but at AUROC 0.668 the corresponding AUPRC sits at the prior and indicates no-skill performance above the base-rate predictor on the precision-recall surface despite above-chance ranking on AUROC. The two metric-relative-to-baseline interpretations should therefore be read independently rather than as parallel indicators of model quality, following McDermott et al. [2024]; AUPRC values should be read against the 0.672 base rate rather than the 0.500 AUROC random-baseline. Per-architecture AUPRC values are reported in Appendix K. Eligibility filters defining the four evaluation cohorts (LOTO at 65 targets, LOFO at 61 targets, within-target cross-lab at 36 targets) are reported in Table 1. The E3-ligase distribution is heavily skewed (CRBN $n=7727$, VHL $n=2896$, other $n=125$), motivating the cross-E3 robustness analysis in Appendix K. A scaffold-split alternative was considered and rejected: 5-fold scaffold cross-validation reaches 0.897 AUROC, statistically indistinguishable from random cross-validation at 0.902. Under 5-fold scaffold-CV, 99.6 percent of test compounds share their target with at least one training compound (vs 0 percent under LOTO); 88 of 173 targets appear in all five scaffold folds. The 7,427 unique Murcko scaffolds across 10,748 compounds (Table 1) leave same-target compounds distributed across many distinct scaffolds, so a scaffold split does not isolate targets and the chemical-novelty shift that LOTO enforces is not reproduced. LOTO is therefore adopted as the canonical evaluation protocol throughout.

PROTAC-Bench is not in competition on raw size with the larger catalogue-style compendia: TPDdb Qin et al. [2026] (October 2025, 22,183 entries) and PROTAC-PatentDB Cai et al. [2025] (November 2025, 63,136 patent compounds) substantially exceed PROTAC-Bench in compound count but yield only 10 LOTO-evaluable targets in TPDdb under PROTAC-Bench’s eligibility filters versus

65 in PROTAC-Bench, since most of their volume derives from patent enumeration without per-target activity depth (Appendix K, Table 11). PROTAC-Bench’s distinguishing curation feature is within-target measurement density and multi-publication replicate structure: the 36-target cross-laboratory cohort with at least three publications per target enables the inter-laboratory variance attribution in Section 5, and a reusable dual-LLM metadata-enrichment pipeline (Appendix H) recovers cell-line, readout-method, timepoint, and concentration annotations on 70.9 percent of the source corpus.

Table 1: PROTAC-Bench dataset summary.

Property	Value
Total entries	10,748
Unique targets (UniProt)	173
LOTO-eligible targets ($n \geq 10$, pos rate $\in [0.1, 0.9]$)	65
LOFO-eligible targets (covered by 22-family map)	61
Cross-lab eligible targets (≥ 3 papers, ≥ 5 entries each)	36
E3 ligase distribution	CRBN 7,727 / VHL 2,896 / other 125
Activity rate (full benchmark / LOTO cohort)	0.658 / 0.672
Label criterion	DC50 < 1 μ M OR Dmax > 50%
Unique Murcko scaffolds (singletons)	7,427 (5,771)

3.2 Evaluation Protocol

Four primary evaluation splits are defined, with random cross-validation referenced as the published-AUROC baseline only. LOTO removes all entries for one held-out UniProt target from training and evaluates the model on the held-out target. LOFO removes all entries for one held-out protein family, providing a stricter test of structural generalisation. Temporal-prospective evaluation trains on entries from publications before 2023 and tests on 2024 entries. Within-target cross-lab evaluation holds out one publication’s entries within each multi-publication target, providing the inter-laboratory measurement-variance anchor for Section 5. The canonical evaluation metric is macro-mean AUROC across held-out folds rather than pooled AUROC, since the held-out-target deployment regime is target-distributional rather than compound-distributional; the choice and its consequences for the gap decomposition are detailed in Section 5. The split hierarchy under matched canonical RF settings is: random CV pooled at 0.902, scaffold CV at 0.897, LOTO macro-mean at 0.668, LOFO macro-mean at 0.616.

3.3 Baseline and Released Artefacts

The canonical baseline is RandomForestClassifier (n_estimators=200, min_samples_leaf=3, class_weight=balanced) applied to 2048-bit Morgan fingerprints at radius 2, evaluated across 10 canonical seeds {7, 13, 29, 42, 43, 44, 53, 71, 89, 97}. The 10-seed validated LOTO macro-mean AUROC is 0.668 ± 0.005 with 95 percent CI [0.664, 0.672]. Ten seeds were chosen because per-target heterogeneity (approximately 0.19 standard deviation across the 65-target cohort) dominates seed stochasticity (approximately 0.005). Fingerprint configuration is largely insensitive to choice: 15 radius/bit-width combinations yield results within 0.01 AUROC of canonical. The released artefacts comprise the dataset CSV, fold assignment files for the four primary evaluation splits (LOTO, LOFO, temporal-prospective, within-target cross-lab), the dual-LLM-enriched metadata file, evaluation code, and Croissant metadata at MLCommons Croissant 1.0 schema compliance with all twenty MLCommons RAI extension fields populated (validation detail in Appendix P). The dataset is hosted at <https://huggingface.co/datasets/ThorK1/protac-bench> under CC-BY-4.0. The evaluation code and reproducibility scripts are hosted on GitHub at <https://github.com/ThorK1m/PROTAC-Bench> under MIT. A reusable dual-LLM metadata-enrichment pipeline is released alongside the dataset (70.9 percent coverage on the 9,384-row source corpus, full methodology in Appendix H); the reproduce.sh script regenerates canonical results (Appendix P).

4 Universal Architecture Plateau Across Eight Predictors

4.1 Architecture-Invariant Performance Plateau

LOTO performance plateaus within a 0.13 AUROC band across all eight architectures we evaluated. The panel spans published PROTAC models (DeepPROTACs Li et al. [2022], DegradeMaster Liu et al. [2025], the Ribes ProtTrans baseline Ribes et al. [2024]) and standard chemical baselines (Random Forest with Morgan fingerprints, GIN, D-MPNN, ChemBERTa-2); PROTAC-STAN Chen

et al. [2025] is included via partial replication of its ternary-attention component (Appendix O, single-seed 0.718 regressing to 0.656 under 3-seed validation). The architecture-invariance pattern observed here differs from the analogous finding of Xia et al. [2023] under random-CV in being driven by the inter-laboratory measurement-variance ceiling identified in Section 5 rather than by representational adequacy of simple baselines. The largest matched-cohort delta (DegradeMaster on the 19-target intersection of its 27-target cohort with canonical LOTO eligibility, Table 2) is bounded above by +0.024 AUROC under matched 7-seed fast-protocol evaluation, statistically indistinguishable from the canonical baseline under Holm correction across the eight-architecture sweep (Appendix F) and within the 0.124 inter-laboratory variance band documented in Section 5.²

Protein language model (PLM) scaling presents a non-monotonic relationship under LOTO evaluation, with ESM-2 peaking at the 150M parameter scale (0.691) and reduced performance at smaller (8M: 0.674, 35M: 0.665) and larger (650M: 0.667, 3B: 0.656) scales under maximal pretraining overlap (all 65 LOTO-eligible targets at 100 percent UniRef100 identity to the ESM-2 corpus). Larger PLMs do not improve LOTO under this configuration; the result is confounded by leakage and consistent with an accidental-taxonomist mechanism Hallee et al. [2025] in which larger PLMs identify target taxonomy more sharply on a panel they have already seen verbatim. The 0.691 peak at 150M sits within the 0.124 inter-laboratory variance band of Section 5; the architecture-invariance claim is ceiling-bounded rather than pointwise. The methodologically appropriate test of PLM architectural saturation requires UniRef50-cluster-level holdout or masked-cluster training Hermann et al. [2024], Szymborski and Emad [2026] and is deferred to a future revision; the architecture-invariance claim therefore scopes to PLM scale providing no benefit on this maximally-leaked panel rather than to PLM scale providing no benefit in general (full UniRef diagnostic in Appendix A).

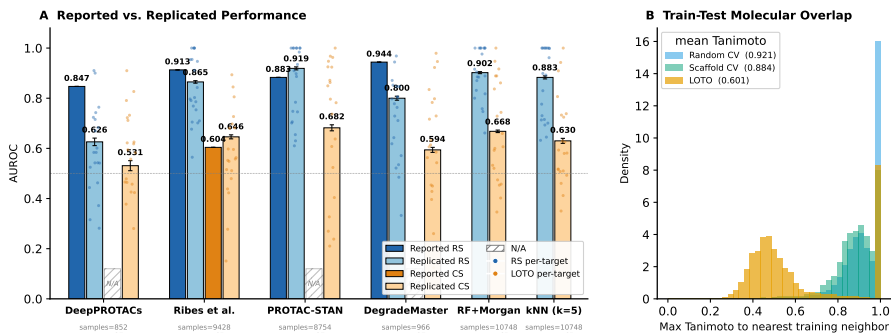


Figure 1: **The held-out-target performance gap and train-test molecular overlap.** (A) Reported versus replicated AUROC across four published PROTAC predictors (DeepPROTACs, Ribes et al., PROTAC-STAN, DegradeMaster) and two reference baselines (RF+Morgan, kNN). Per-target AUROCs are overlaid as scatter dots on the replicated bars. (B) Maximum Tanimoto similarity to nearest training-set neighbor, density across protocols. Random cross-validation yields a tight high-similarity distribution; scaffold cross-validation reduces overlap moderately; LOTO produces a broad low-similarity distribution.

4.2 Hyperparameter Optimisation Cannot Break the Ceiling

We performed a 21-dimensional hyperparameter optimisation across 2,000 trials and find that the ceiling is not broken: the rank-1 single-seed objective of 0.764 regresses to 0.603 ± 0.012 under 5-seed validation, an inflation of 0.161 AUROC of the single-seed objective above the multi-seed-validated mean. Ranks 2 through 10, each validated under 5 canonical seeds, regress to the 0.659 to 0.679 range and are statistically indistinguishable from the canonical RF + Morgan baseline at 0.668 (paired Wilcoxon $p > 0.1$); the rank-1 regression illustrates the Cawley-Talbot selection-bias mechanism while ranks 2 through 10 converge at the architecture-invariance ceiling. Configurations selected by HPO under-represent warhead transfer at 4 percent of top-50 trials versus 36 percent base rate, indicating that single-evaluation HPO does not discover signals requiring multi-seed validation, consistent with Bouthillier et al. [2021]. The 0.161 regression matches the Bailey-López de Prado closed-form maximum-over-trials prediction $E[\max] \approx \sqrt{2 \log N} \sigma = 0.167$ at $N=2000$,

²The eight-architecture panel is protein-encoder-centric; structure-prediction PROTAC variants (BoltzDesign-class, ProteinMPNN-PROTAC) predict ternary geometry rather than activity and are out of scope for the activity-prediction comparison reported here.

Table 2: Architecture invariance under canonical LOTO evaluation. Standard deviations across canonical seeds (3 to 10 depending on architecture). Per-target heterogeneity is approximately 0.19 across all rows. Extended table covering GIN, D-MPNN, and DeepPROTACs is reported in Appendix F. † indicates values reported by original authors under their canonical random-split protocol rather than re-evaluated here. The RF+Morgan row reports $n_{\text{tgt}} = 64$ rather than 65 because one LOTO-eligible target failed per-seed evaluation under the matched canonical-RF settings used for the Table; the Section 3.3 canonical baseline of 0.668 ± 0.005 is computed across all 65 LOTO-eligible targets.

Method	RCV pool	RCV macro	LOTO macro	Δ_{macro}	n_{tgt}
RF + Morgan 2048 r2	0.902 ± 0.001	0.755 ± 0.006	0.668 ± 0.005	-0.087	64
ChemBERTa-2	0.875 ± 0.002	0.717 ± 0.010	0.663 ± 0.008	-0.054	65
Ribes (ProtTrans)	0.913 ± 0.001	0.716 ± 0.007	0.637 ± 0.011	-0.079	65
DegradeMaster (canonical)	$\sim 0.944^\dagger$	0.800^\dagger	0.594 ± 0.014	-0.206	61

$\sigma \approx 0.043$ [Bailey et al., 2014, Bailey and López de Prado, 2014], to within 4 percent under independent-trials assumption (full detail in Appendix B). A continuous SPECTRA-style similarity-resolution sweep Ektefaie et al. [2024] places LOTO at 0.668 below the most restrictive measured similarity threshold ($s = 0.50$, AUROC 0.652; Appendix C).

4.3 Additional Approaches Below the Ceiling

Beyond the eight tabulated architectures, PLM embeddings, EGNN encoders, Boltz-2 ternary structure features Passaro et al. [2025], and 22 metadata-feature variants yield LOTO AUROC within 0.01 of the canonical baseline (Appendices A, G, E, J); the within-target cross-lab cascade $0.802 \rightarrow 0.678 \rightarrow 0.653$ anchors Section 5, with EGNN pocket-shuffle and zero-pocket controls within 0.013 AUROC of original-pocket performance (Appendix G).

5 Variance-Share Decomposition: Inter-Laboratory Variance Sets Most of the Ceiling

We decompose the gap, anchor each component empirically, and test the dominance ordering. The within-target cross-lab cascade attributes a 0.124 AUROC bound to inter-laboratory measurement effects (random-CV 0.802, cross-lab 0.678, LOTO 0.653 on the 36-target cohort, paired $n = 35$), with a complementary target-clustered variance-share analysis assigning $\omega^2 = 0.256$ of cohort variance to the target facet under bias correction (95 percent CI [0.110, 0.421], target heterogeneity inclusive of inter-laboratory variance). The unbiased ω^2 values are reported as primary because eta-squared is upward-biased at small n Okada [2013]; negative ω^2 values, which appear for the laboratory-times-binarisation interaction term under the small- n bias correction, indicate effects statistically indistinguishable from zero rather than numerical errors and should be read as zero (full ANOVA tabulation including eta-squared corroboration and interaction-term detail in Appendix K). The 0.124 inter-laboratory anchor itself is supported by a target-clustered bootstrap 95 percent CI of [0.0512, 0.1971] and leave-one-target-out sensitivity range [0.1132, 0.1308] across the 12 replicate-bearing targets (Appendix K).

The variance-share analysis is triangulated by four independent measurement-protocol bounds: the 0.124 AUROC inter-laboratory bound from the cross-lab cascade on the 36-target cohort (random-CV 0.802, cross-lab 0.678, LOTO 0.653; median 3.7-fold cross-lab DC50 change on identical compounds, Appendix K); the 0.05 binarisation spread across four labelling schemes; the 0.008 cross-DOI conflict-removal contribution; and the 0.02 to 0.03 residual LOTO distributional shift (Appendix L). The cross-lab anchor dominates; remaining contributions sit within the small- n bias correction or seed noise. The alternative inherent-difficulty interpretation is inconsistent with the SPECTRA sweep at $s = 0.50$ (AUROC 0.652, Appendix C) and with the within-target cross-lab evaluation at 0.678 under removed structural shift. Cross-lab same-compound pairs are retained without deduplication because identical compounds measured across publications are the empirical signal anchoring the variance estimate (Appendix K, 28 cross-paper comparisons across 12 replicate-bearing targets, median 3.7-fold).

Three closely related views of the LOTO ceiling fall in the 0.668 to 0.678 range under similar aggregation choices, identifying inter-laboratory measurement variance as accounting for 0.117 of the 0.149 AUROC random-CV-to-LOTO gap on the 36-target cross-laboratory cohort (approximately 81 percent), and a comparable fraction of the smaller 65-target macro-gap of 0.087 under family-

composition transfer (Appendix K). The per-target standard deviation of LOTO AUROC across the 65-target cohort is 0.190, reported separately in Appendix N as a per-target variance measure rather than as a between-protocol gap. The dominance argument rests on partially-overlapping bounds rather than a strict additive identity: the four anchors (0.124, 0.05, 0.008, 0.02 to 0.03) sum to approximately the 0.18 to 0.20 macro-mean gap as a coarse upper-bound triangulation, and the variance-to-AUROC translation is empirically anchored by the Appendix L synthetic-noise calibration (0.124 bound projects to 21 to 27 percent equivalent flip rate across three noise models). The roughly 80 to 85 percent attribution is conditional on within-cohort identification. The decomposition predicts that per-target calibration with a small number of measured compounds recovers the inter-laboratory variance component; Section 6 confirms this empirically.

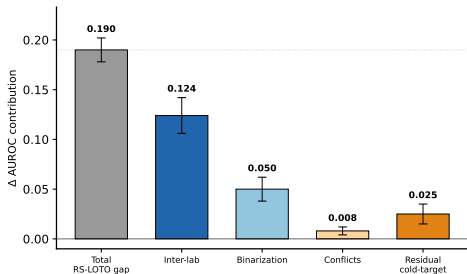


Figure 2: **Triangulating bounds on the random-CV-to-LOTO gap.** Methodologically primary decomposition is the $\omega^2 = 0.256$ variance-share analysis reported in the body text; bars are partially-overlapping bounds rather than additive components (the four anchors sum to approximately the 0.18 to 0.20 macro-mean gap as a coarse upper-bound triangulation rather than as an additive identity).

Same-compound-cross-target sensitivity. SMILES-level deduplication of the LOTO training partition drops the canonical 65-target macro-mean LOTO AUROC by 0.051 ± 0.007 (paired Wilcoxon $p = 0.002$, 10 seeds), translating the canonical 0.668 ceiling to a dedup-protocol ceiling of approximately 0.617 AUROC. The 0.124 inter-laboratory cascade bound is anchored on within-target same-compound replicate measurements rather than cross-target leakage; the cascade ordering is preserved under SMILES deduplication with absolute AUROCs shifting by approximately 0.05 across both protocols (Appendix K).

6 Few-Shot Calibration Recovers Within-Ceiling Performance

6.1 Factorial Decomposition

The Section 5 decomposition predicts that per-target calibration should recover the inter-laboratory variance component. We test this via a $2 \times 2 \times 2 \times 2$ factorial design across four pipeline factors (Morgan fingerprints M, warhead transfer W, ADMET features A, few-shot $k=5$ stratified per-target calibration K) under 10-seed canonical evaluation, with marginal contributions evaluated against a Morgan-anchored common reference rather than in isolated four-bar ablations (Appendix I). Marginal contributions are reported in Figure 3A: few-shot calibration contributes $+0.0306$ with 95 percent CI $[+0.015, +0.051]$, ADMET $+0.0111$ with CI $[+0.004, +0.019]$, warhead transfer $+0.0025$ with CI $[-0.009, +0.015]$ crossing zero. Few-shot calibration is the only factor whose marginal contribution is bounded away from zero across all four paired comparisons; the previously headlined cross-target warhead-transfer effect of $+0.042$, observed under isolated four-bar ablation, shrinks to within seed standard deviation when decomposed against few-shot calibration in the same factorial design. The pre-specified minimum detectable effect at 80 percent power and $\alpha = 0.05$ is 0.0178 AUROC for the warhead contrast at empirical ICC $\rho = 0.293$ and 0.0260 for the few-shot contrast at empirical ICC $\rho = 0.472$; both findings are informative at the empirical ICC values rather than underpowered, indicating that the apparent warhead-transfer effect under isolated ablation reflected an unmodelled few-shot signal rather than a warhead-specific contribution. Full ICC sensitivity grids across the pre-specified $\rho \in \{0.10, 0.20, 0.30, 0.40\}$ range plus the empirical ICC row for each contrast are reported in Tables 7 and 8 (Appendix I); the warhead effect sits below the MDE across the entire grid, while the few-shot effect exceeds the MDE at the empirical ICC and across the lower-ICC range.

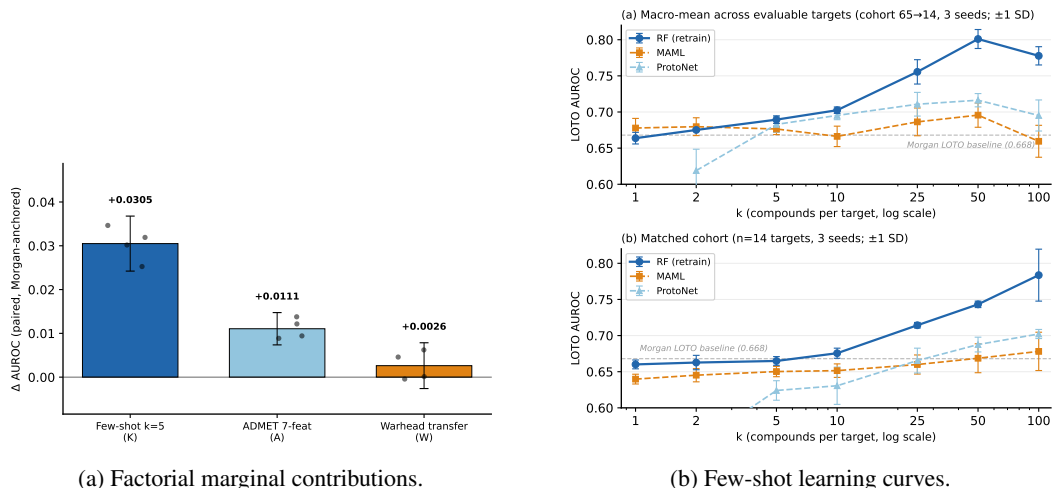


Figure 3: **Factorial decomposition and few-shot calibration.** (a) Mean marginal AUROC contribution of each factor under target-clustered bootstrap ($n=65$ targets, 5000 replicates); few-shot $k=5$ at $+0.0306$ with CI $[+0.015, +0.051]$, ADMET at $+0.0111$, warhead transfer at $+0.0025$ with CI $[-0.009, +0.015]$ crossing zero. (b) Few-shot learning curves: RF retraining beats both meta-learning baselines (MAML, ProtoNet) at every k ; the dashed horizontal line at 0.668 marks the canonical Morgan baseline.

6.2 Few-Shot Calibration Outperforms Meta-Learning Baselines

We implement few-shot calibration as per-target retraining on k stratified compounds selected by predicted-probability quintiles, contrasted with two meta-learning baselines (MAML and ProtoNet with Tanimoto distance). The per-target sampling protocol stratifies on the binary activity label and excludes selected compounds from the test fold to prevent same-compound train-test contamination; protocol details and per-target sample-size statistics are reported in Appendix I.1. RF retraining on the matched 14-target cohort reaches 0.7126 at $k=25$, 0.743 ± 0.012 at $k=50$, and 0.778 ± 0.023 at $k=100$, with the within-cohort improvement of $+0.114$ AUROC at $k=100$ (95 percent CI $[+0.079, +0.152]$) confirming a genuine signal rather than a cohort-restriction artefact; the non-saturating curve at $k=100$ indicates the asymptotic ceiling is meaningfully above 0.743. MAML and ProtoNet plateau or regress past $k=25$, indicating that the extended-regime gain is RF-specific and consistent with the simple-baseline pattern documented across the few-shot literature Tian et al. [2020], Chen et al. [2019], Stanley et al. [2021]. Stratified quintile sampling outperforms random sampling at $k=5$ under paired comparison; full per-quintile breakdown is deferred to a future revision.

6.3 Practical Recommendation and Applicability Domain

The deployment protocol is a three-tier progression on the 65-target LOTO cohort: Morgan baseline (no per-target retraining) 0.668 ± 0.005 ; Morgan plus ADMET (zero-cost addition of seven TDC-trained classifiers) 0.687 ± 0.005 ; Morgan plus ADMET plus $k=5$ stratified per-target retraining 0.7050 ± 0.0042 (Table 6 cell 1011). The matched-cohort 14-target curve in Section 6.2 reaches 0.743 ± 0.012 at $k=50$ and 0.778 at $k=100$ on a continuous-DC₅₀ subcohort; these are upper-bound proxies on the deployment-relevant apples-to-apples headline rather than cohort-matched figures.³ The few-shot-recovered 0.743 is a within-time-period upper bound under stratified-quintile selection; prospective validation is currently underpowered (5-target 2024 cohort at 0.674, cannot distinguish null from a benefit up to approximately 0.10 AUROC under 80 percent power), so the prospective benefit reads as promising but preliminary until expanded panels permit definitive evaluation. Deployment regime determines achievable performance: stratified-quintile selection requires existing predictions and reaches 0.743 at $k=5$; random-compound selection costs approximately 0.01 to 0.02 AUROC; medicinal-chemistry-constrained selection (compound availability dictates the k measured) is expected at intermediate performance and is the appropriate prospective-benchmarking target. Per-target AUROC varies substantially across families: one-way ANOVA grouped by the 22-family map ($F(22, 627) = 6.04, p < 10^{-15}$) attributes $\omega_{\text{family}}^2 = 0.146$ of seed-level variance (95 percent CI

³Per-target retraining improves discrimination but not probability calibration; raw output ECE is unchanged under this protocol (Appendix M). Probability-calibration recovery via post-hoc Platt scaling is treated separately in Section 7.

[0.094, 0.399]; η^2 corroboration and per-family detail in Appendix N); ranking accuracy will differ across families even after Platt scaling.

7 Discussion

The architecture-cap claim rests on two convergent observations: the rank-1 HPO single-seed configuration regresses by 0.161 AUROC under 5-seed validation in agreement with the Bailey-López de Prado prediction Bailey et al. [2014], Bailey and López de Prado [2014], Cawley and Talbot [2010], and the factorial decomposition shrinks an apparent cross-target warhead-transfer effect of +0.042 to within seed standard deviation once the factor is evaluated alongside few-shot per-target retraining. The interpretation does not imply that LOTO PROTAC activity prediction has been solved (the inter-laboratory component is itself a learning challenge for prospective deployment), but it does imply that gains from larger models or more aggressive hyperparameter optimisation will be capped at the inter-laboratory reproducibility floor of 0.668 to 0.678 AUROC.

Cross-E3 transfer is asymmetric: CRBN-trained models reach 0.606 AUROC on VHL, VHL-trained reach 0.643 on CRBN; the originally-reported asymmetry largely reflects training-set size differences and shrinks under matched-size resampling (Appendix K). The absolute-performance asymmetry persists; the direction differs from Riepenhausen et al. [2026]’s structural-prediction finding that VHL-mediated ternary complexes are predicted more accurately than CRBN, suggesting activity-prediction transfer asymmetry and structural-prediction accuracy are decoupled on this cohort.

For deployment, Platt scaling is the recommended calibrator: it recovers raw output ECE-10 from 0.150 to 0.031 ± 0.002 , below the 0.05 well-calibrated threshold in all 10 of 10 seeds. Temperature scaling reduces ECE-10 but does not cross the 0.05 threshold while Platt’s two-parameter form does, consistent with the dataset-shift overconfidence pattern documented by Ovadia et al. [2019]; Platt’s two-parameter form gains its ECE advantage at the high-confidence tail where the empirical-versus-predicted gap is largest [Jones et al., 2020] (Appendix M). Under raw output the practical claim is bounded to active-versus-inactive enrichment; Platt-scaled probabilities additionally support decision-theoretic use under heterogeneous costs and probability thresholds.

Published architecture advantages reduce to data curation under matched evaluation: DegradeMaster’s advantage shrinks to +0.024 AUROC under fast-protocol matched-cohort evaluation and reverses to -0.086 under canonical full-protocol replication (Appendix F); the DeepPROTACs 0.221 gap decomposes into upstream curation choices (Appendix D).

Limitations. Five limitations are worth flagging. First, evaluation is restricted to binary classification: the same features that improve binary AUROC produce a point estimate of continuous-DC50 Spearman degradation from 0.38 to 0.30, suggestive of classification-ranking divergence but not statistically significant under target-clustered inference (95 percent CI $[-0.221, +0.032]$, $p = 0.198$) at the limiting 16-target continuous-DC50 cohort, so the practical claim is bounded to active-versus-inactive enrichment until expanded continuous panels permit a definitive regression evaluation. Second, the PLM scaling result scopes to ESM-2 evaluated on a panel where every target appears in the pretraining corpus at UniRef100 identity; the architecture-invariance claim does not extend to PLMs on UniRef50-cluster-level held-out targets (Appendix A). Third, LOFO evaluation reaches AUROC 0.616 ± 0.024 , approximately 0.046 below LOTO, within the inter-laboratory measurement-variance band; the implied clean-cohort LOTO ceiling is 0.693 after pathological-tail correction (Appendix N). Fourth, the dataset is heavily skewed toward CRBN-recruited PROTACs ($n=7727$ versus VHL $n=2896$, other $n=125$), constraining generalisability to non-CRBN E3 ligases. Fifth, SMILES-level deduplication of the LOTO training partition drops the canonical 0.668 ceiling by approximately 0.051 AUROC; the deduplicated 0.617 figure is the more conservative reproducibility-anchored generalisation floor (Section 5, Appendix K).

8 Conclusion

The held-out-target ceiling for PROTAC activity prediction sits at approximately 0.668 AUROC across every architecture, PLM scale, and hyperparameter configuration we evaluated; target-clustered variance-share decomposition attributes $\omega^2 = 0.256$ of variance to the target facet (95 percent CI $[0.110, 0.421]$), with the laboratory-specific component anchored at 0.124 AUROC by the cross-lab cascade, placing the apparent generalisation gap in the measurement-variance regime rather than the learning-failure regime Burnett et al. [2024], Pahikkala et al. [2015], Haibe-Kains et al. [2013], Roberts et al. [2017]. Few-shot $k=5$ stratified per-target retraining combined with ADMET features lifts 65-target LOTO AUROC from 0.668 to 0.7050 and Platt scaling recovers raw ECE from 0.150

to 0.031 ± 0.002 . We release PROTAC-Bench and the variance-decomposition framework as a methodological template for similar variance attributions in other small-data therapeutic settings.

Acknowledgments and Disclosure of Funding

This work received no external funding. All compute, cloud infrastructure, API costs, and research time were privately funded by the first author (T.K.); neither L3S Research Center nor Leibniz Universität Hannover provided financial support for this project, and the affiliations indicate current academic placement rather than institutional sponsorship of the work reported here. Total cost is on the order of a few hundred USD, and was fully privately funded by the first author, comprising approximately three weeks of Vast.ai GPU rental on a $2 \times$ NVIDIA RTX 4090 instance at on-demand pricing and under 10 USD of large language model API spend for the metadata-enrichment pipeline described in Appendix H.

We thank W.N. and M.T. for scientific guidance throughout the project. We acknowledge the upstream curation efforts that PROTAC-Bench builds upon: the PROTAC-Degradation-Predictor curation of Ribes et al. [2024] (MIT licence), PROTAC-DB 3.0 of Ge et al. [2025] (CC-BY-4.0), and the DegradeMaster curated subset of Liu et al. [2025].

LLM usage in this work spans three categories: editing assistance (grammar, spelling, word choice), implementing methods where the LLM plays an original, non-standard role, and understanding technical concepts. Specifically, a dual-LLM extraction pipeline (Anthropic Claude Haiku 4.5 and OpenAI GPT-4.1) was used for structured metadata enrichment from PubMed abstracts, open-access full-text articles, and ChEMBL records; the two models produced independent extractions reconciled to populate fields including cell lines, species, readout methods, timepoints, and concentrations.

Open-access funding via Projekt DEAL is not applicable to this work. The authors declare no competing financial or non-financial interests.

References

- John Arevalo, Ellen Su, Anne E Carpenter, and Shantanu Singh. Motive: A drug-target interaction graph for inductive link prediction. *Advances in Neural Information Processing Systems*, 37: 140320–140333, 2024.
- David H Bailey and Marcos López de Prado. The deflated sharpe ratio: Correcting for selection bias, backtest overfitting and non-normality. *Journal of Portfolio Management*, 40(5):94–107, 2014.
- David H Bailey, Jonathan M Borwein, Marcos López De Prado, and Qiji Jim Zhu. Pseudomathematics and financial charlatanism: The effects of backtest over fitting on out-of-sample performance. *Notices of the AMS*, 61(5):458–471, 2014.
- Judith Bernett, David B Blumenthal, and Markus List. Cracking the black box of deep sequence-based protein–protein interaction prediction. *Briefings in Bioinformatics*, 25(2):bbae076, 2024.
- Xavier Bouthillier, Pierre Delaunay, Mirko Bronzi, Assya Trofimov, Brennan Nichyporuk, Justin Szeto, Nazanin Mohammadi Sepahvand, Edward Raff, Kanika Madan, Vikram Voleti, et al. Accounting for variance in machine learning benchmarks. *Proceedings of machine learning and systems*, 3:747–769, 2021.
- Hong Cai, Gengyuan Yao, Yulong Shi, Tianyi Zhang, and Yuanjia Hu. Protac-patentdb: A protac patent compound dataset. *Scientific Data*, 12(1):1840, 2025.
- Gavin C Cawley and Nicola LC Talbot. On over-fitting in model selection and subsequent selection bias in performance evaluation. *The Journal of Machine Learning Research*, 11:2079–2107, 2010.
- Wei-Yu Chen, Yen-Cheng Liu, Zsolt Kira, Yu-Chiang Frank Wang, and Jia-Bin Huang. A closer look at few-shot classification. *arXiv preprint arXiv:1904.04232*, 2019.
- Zhenglu Chen, Chunbin Gu, Shuoyan Tan, Xiaorui Wang, Yuquan Li, Mutian He, Ruiqiang Lu, Shijia Sun, Chang-Yu Hsieh, Xiaojun Yao, et al. Interpretable protac degradation prediction with structure-informed deep ternary attention framework. *Advanced Science*, 12(47):e08138, 2025.
- Xingyi Cheng, Bo Chen, Pan Li, Jing Gong, Jie Tang, and Le Song. Training compute-optimal protein language models. *Advances in Neural Information Processing Systems*, 37:69386–69418, 2024.

- Lee Joseph Cronbach. The dependability of behavioral measurements. *Theory of generalizability for scores and profiles*, pages 1–33, 1972.
- Alexander D’Amour, Katherine Heller, Dan Moldovan, Ben Adlam, Babak Alipanahi, Alex Beutel, Christina Chen, Jonathan Deaton, Jacob Eisenstein, Matthew D Hoffman, et al. Underspecification presents challenges for credibility in modern machine learning. *Journal of Machine Learning Research*, 23(226):1–61, 2022.
- Jianyuan Deng, Zhibo Yang, Hehe Wang, Iwao Ojima, Dimitris Samaras, and Fusheng Wang. A systematic study of key elements underlying molecular property prediction. *Nature Communications*, 14(1):6395, 2023.
- Nils Dunlop, Francisco Erazo, Farzaneh Jalalypour, and Rocío Mercado. Predicting protac-mediated ternary complexes with alphafold3 and boltz-1. *Digital Discovery*, 4(12):3782–3809, 2025.
- Yasha Ektefaie, Andrew Shen, Daria Bykova, Maximillian G Marin, Marinka Zitnik, and Maha Farhat. Evaluating generalizability of artificial intelligence models for molecular datasets. *Nature Machine Intelligence*, 6(12):1512–1524, 2024.
- Jingxuan Ge, Shimeng Li, Gaoqi Weng, Huating Wang, Meijing Fang, Huiyong Sun, Yafeng Deng, Chang-Yu Hsieh, Dan Li, and Tingjun Hou. Protac-db 3.0: an updated database of protacs with extended pharmacokinetic parameters. *Nucleic Acids Research*, 53(D1):D1510–D1515, 2025. doi: 10.1093/nar/gkae768.
- Robert Geirhos, Jörn-Henrik Jacobsen, Claudio Michaelis, Richard Zemel, Wieland Brendel, Matthias Bethge, and Felix A Wichmann. Shortcut learning in deep neural networks. *Nature Machine Intelligence*, 2(11):665–673, 2020.
- David Graber, Peter Stockinger, Fabian Meyer, Siddhartha Mishra, Claus Horn, and Rebecca Buller. Resolving data bias improves generalization in binding affinity prediction. *Nature Machine Intelligence*, pages 1–13, 2025.
- Jiaqi Guan, Xingang Peng, PeiQi Jiang, Yunan Luo, Jian Peng, and Jianzhu Ma. Linkernet: Fragment poses and linker co-design with 3d equivariant diffusion. *Advances in Neural Information Processing Systems*, 36:77503–77519, 2023.
- Ishaan Gulrajani and David Lopez-Paz. In search of lost domain generalization. *arXiv preprint arXiv:2007.01434*, 2020.
- Benjamin Haibe-Kains, Nehme El-Hachem, Nicolai Juul Birkbak, Andrew C Jin, Andrew H Beck, Hugo JWL Aerts, and John Quackenbush. Inconsistency in large pharmacogenomic studies. *Nature*, 504(7480):389–393, 2013.
- Logan Hallee, Tamar Peleg, Nikolaos Rafailidis, and Jason P Gleghorn. Protein language models are accidental taxonomists. *bioRxiv*, pages 2025–10, 2025.
- Leon Hermann, Tobias Fiedler, Hoang An Nguyen, Melania Nowicka, and Jakub M Bartoszewicz. Beware of data leakage from protein llm pretraining. *bioRxiv*, pages 2024–07, 2024.
- Roman Joeres, David B Blumenthal, and Olga V Kalinina. Data splitting to avoid information leakage with datasail. *Nature Communications*, 16(1):3337, 2025.
- Erik Jones, Shiori Sagawa, Pang Wei Koh, Ananya Kumar, and Percy Liang. Selective classification can magnify disparities across groups. *arXiv preprint arXiv:2010.14134*, 2020.
- Ananya Kumar, Aditi Raghunathan, Robbie Jones, Tengyu Ma, and Percy Liang. Fine-tuning can distort pretrained features and underperform out-of-distribution. *arXiv preprint arXiv:2202.10054*, 2022.
- Alexandre Lacoste, Alexandra Luccioni, Victor Schmidt, and Thomas Dandres. Quantifying the carbon emissions of machine learning. *arXiv preprint arXiv:1910.09700*, 2019.
- Gregory A Landrum and Sereina Riniker. Combining ic50 or k_i values from different sources is a source of significant noise. *Journal of chemical information and modeling*, 64(5):1560–1567, 2024.

- Baiqing Li, Ting Ran, and Hongming Chen. 3d based generative protac linker design with reinforcement learning. *Briefings in bioinformatics*, 24(5):bbad323, 2023.
- Fenglei Li, Qiaoyu Hu, Xianglei Zhang, Renhong Sun, Zhuanghua Liu, Sanan Wu, Siyuan Tian, Xinyue Ma, Zhizhuo Dai, Xiaobao Yang, et al. Deepprotacs is a deep learning-based targeted degradation predictor for protacs. *Nature communications*, 13(1):7133, 2022.
- Fenglei Li, Qiaoyu Hu, Yongqi Zhou, Hao Yang, and Fang Bai. Diffprotacs is a deep learning-based generator for proteolysis targeting chimeras. *Briefings in bioinformatics*, 25(5):bbae358, 2024.
- Zeming Lin, Halil Akin, Roshan Rao, Brian Hie, Zhongkai Zhu, Wenting Lu, Nikita Smetanin, Robert Verkuil, Ori Kabeli, Yaniv Shmueli, et al. Evolutionary-scale prediction of atomic-level protein structure with a language model. *Science*, 379(6637):1123–1130, 2023.
- Jie Liu, Michael J Roy, Luke Isbel, and Fuyi Li. Accurate protac-targeted degradation prediction with degrademaster. *Bioinformatics*, 41(Supplement_1):i342–i351, 2025.
- Yunchao Liu, Ha Dong, Xin Wang, Rocco Moretti, Yu Wang, Zhaoqian Su, Jiawei Gu, Bobby Bodenheimer, Charles D Weaver, Jens Meiler, et al. Welqrate: defining the gold standard in small molecule drug discovery benchmarking. *Advances in Neural Information Processing Systems*, 37: 53222–53236, 2024.
- Matthew B McDermott, Haoran Zhang, Lasse H Hansen, Giovanni Angelotti, and Jack Gallifant. A closer look at auROC and aupRC under class imbalance. *Advances in Neural Information Processing Systems*, 37:44102–44163, 2024.
- Kensuke Okada. Is omega squared less biased? a comparison of three major effect size indices in one-way ANOVA. *Behaviormetrika*, 40(2):129–147, 2013.
- Yaniv Ovadia, Emily Fertig, Jie Ren, Zachary Nado, David Sculley, Sebastian Nowozin, Joshua Dillon, Balaji Lakshminarayanan, and Jasper Snoek. Can you trust your model’s uncertainty? evaluating predictive uncertainty under dataset shift. *Advances in neural information processing systems*, 32, 2019.
- Tapio Pahikkala, Antti Airola, Sami Pietilä, Sushil Shakyawar, Agnieszka Szwejda, Jing Tang, and Tero Aittokallio. Toward more realistic drug–target interaction predictions. *Briefings in bioinformatics*, 16(2):325–337, 2015.
- Yungki Park and Edward M Marcotte. Flaws in evaluation schemes for pair-input computational predictions. *Nature methods*, 9(12):1134–1136, 2012.
- Saro Passaro, Gabriele Corso, Jeremy Wohlwend, Mateo Reveiz, Stephan Thaler, Vignesh Ram Somnath, Noah Getz, Tally Portnoi, Julien Roy, Hannes Stark, et al. Boltz-2: Towards accurate and efficient binding affinity prediction. *BioRxiv*, 2025.
- Judea Pearl and Elias Bareinboim. External validity: From do-calculus to transportability across populations. *Statistical Science*, 29(4):579–595, 2014.
- Xinran Qin, Yinpeng Zhang, Yajunzi Wang, Yintao Zhang, Jiachen Jing, Yuyuan Zhang, Gaoxiang Xu, Haoping Teng, Tianjun Wang, Lei Fu, et al. TpdDB: the comprehensive database of targeted protein degrader. *Nucleic Acids Research*, 54(D1):D1683–D1691, 2026. doi: 10.1093/nar/gkaf996.
- Stefano Ribes, Eva Nittinger, Christian Tyrchan, and Rocío Mercado. Modeling protac degradation activity with machine learning. *Artificial Intelligence in the Life Sciences*, 6:100104, 2024.
- Lino Riepenhausen, Anne-Christin Sarnow, Dina Robaa, and Wolfgang Sippl. AI-based prediction of protac- and molecular glue-mediated ternary complexes: A comparative evaluation of AlphaFold 3 and Boltz-2. *Archiv der Pharmazie*, 359(3):e70225, 2026. doi: 10.1002/ardp.70225.
- David R Roberts, Volker Bahn, Simone Ciuti, Mark S Boyce, Jane Elith, Gurutzeta Guillera-Arroita, Severin Hauenstein, José J Lahoz-Monfort, Boris Schröder, Wilfried Thuiller, et al. Cross-validation strategies for data with temporal, spatial, hierarchical, or phylogenetic structure. *Ecography*, 40(8):913–929, 2017.

- Megan Stanley, John F Bronskill, Krzysztof Maziarz, Hubert Misztela, Jessica Lanini, Marwin Segler, Nadine Schneider, and Marc Brockschmidt. Fs-mol: A few-shot learning dataset of molecules. In *Thirty-fifth Conference on Neural Information Processing Systems Datasets and Benchmarks Track (Round 2)*, 2021.
- Simon Steshin. Lo-hi: Practical ml drug discovery benchmark. *Advances in Neural Information Processing Systems*, 36:64526–64554, 2023.
- Joseph Szymborski and Amin Emad. A flaw in using pretrained protein language models in protein–protein interaction inference models. *Nature Machine Intelligence*, pages 1–12, 2026. doi: 10.1038/s42256-025-01176-7.
- Yonglong Tian, Yue Wang, Dilip Krishnan, Joshua B Tenenbaum, and Phillip Isola. Rethinking few-shot image classification: a good embedding is all you need? In *European conference on computer vision*, pages 266–282. Springer, 2020.
- Prudencio Tossou, Cas Wognum, Michael Craig, Hadrien Mary, and Emmanuel Noutahi. Real-world molecular out-of-distribution: Specification and investigation. *Journal of Chemical Information and Modeling*, 64(3):697–711, 2024.
- Genta Indra Winata, David Anugraha, Emmy Liu, Alham Fikri Aji, Shou-Yi Hung, Aditya Parashar, Patrick Amadeus Irawan, Ruochen Zhang, Zheng-Xin Yong, Jan Christian Blaise Cruz, et al. Datasheets aren’t enough: Datarubrics for automated quality metrics and accountability. *arXiv preprint arXiv:2506.01789*, 2025.
- Jun Xia, Lecheng Zhang, Xiao Zhu, Yue Liu, Zhangyang Gao, Bozhen Hu, Cheng Tan, Jiangbin Zheng, Siyuan Li, and Stan Z Li. Understanding the limitations of deep models for molecular property prediction: Insights and solutions. *Advances in Neural Information Processing Systems*, 36:64774–64792, 2023.
- Fanglei Xue, Meihan Zhang, Shuqi Li, Xinyu Gao, James A Wohlschlegel, Wenbing Huang, Yi Yang, and Weixian Deng. Se (3)-equivariant ternary complex prediction towards target protein degradation. *Nature Communications*, 16(1):5514, 2025.
- Shuo Yan, Yuliang Yan, Bin Ma, Chenao Li, Haochun Tang, Jiahua Lu, Minhua Lin, Yuyuan Feng, Hui Xiong, and Enyan Dai. Protap: A benchmark for protein modeling on realistic downstream applications. *arXiv preprint arXiv:2506.02052*, 2025.
- Tal Yarkoni. The generalizability crisis. *Behavioral and Brain Sciences*, 45:e1, 2022.

Appendix

Appendix contents.

- **A.** PLM Scaling Diagnostic (page 14)
- **B.** HPO V2 Search Space and Validation (page 14)
- **C.** Continuous Similarity-Resolution Sweep (page 16)
- **D.** DeepPROTACs Gap Reconciliation (page 16)
- **E.** Geometric and Structural Approaches (page 17)
- **F.** DegradeMaster Investigation (page 19)
- **G.** EGNN and Pocket-Shuffle Control (page 20)
- **H.** Metadata Enrichment Pipeline (page 20)
- **I.** Per-Cell Factorial Numbers (page 21)
- **J.** 22-Experiment Metadata Ceiling (page 22)
- **K.** Robustness Analyses (page 23)
- **L.** Synthetic-Noise Calibration (page 26)
- **M.** Calibration (page 26)
- **N.** Per-Family LOFO Breakdown (page 27)
- **O.** What Does Not Work (page 28)
- **P.** Reproducibility (page 30)
- **Q.** Ethics Statement (page 30)

A PLM Scaling Diagnostic

ESM-2 protein language models Lin et al. [2023] at five scales (8M, 35M, 150M, 650M, 3B parameters) were evaluated as protein encoders concatenated to Morgan 2048 fingerprints with a Random Forest head, under both random-split and LOTO evaluation, across 5 canonical seeds. Random-CV pooled AUROC inflates monotonically with PLM scale from 0.890 (8M) to 0.914 (3B), while LOTO macro-mean AUROC follows a non-monotonic pattern peaking at the 150M scale (0.691) with reduced performance at smaller (8M: 0.674, 35M: 0.665) and larger (650M: 0.667, 3B: 0.656) extremes. The BERT-BFD encoder reaches 0.642 LOTO with paired Wilcoxon $p = 0.038$ versus the no-PLM Morgan-only baseline. The mechanism is consistent with the accidental-taxonomist observation of Hallee et al. [2025]: larger PLMs encode species and family identity more sharply, so the held-out target is identified more confidently as a member of a family the model has memorised. A direct UniRef diagnostic on the 65 LOTO targets confirms maximal pretraining-leakage signal: all 65 targets are UniRef100 representatives at 100 percent sequence identity, 61 of 65 occupy UniRef50 clusters of size at least 100, the median UniRef50 cluster size is 481, and 57 of 65 targets share their UniRef50 cluster with at least 5 human paralogs or isoforms. The PLM scaling result therefore cannot be interpreted as out-of-distribution generalization; the 3B-parameter regression under LOTO is consistent with sharper target-identification on a panel where every test target has been seen verbatim during MLM pretraining. The PLM scaling relationship is therefore inverted under LOTO evaluation relative to within-distribution evaluation, with the inversion mechanism mechanistically anchored by the UniRef diagnostic rather than by architectural saturation alone.

B HPO V2 Search Space and Validation

We constructed a 21-dimensional hyperparameter optimisation search space spanning head architecture (RF, XGBoost, MLP, Ridge), seven molecular encoders (Morgan at five bit widths, MolFormer, ChemBERTa), eight protein encoders (no-protein baseline plus six ESM-2 scales from 8M to 3B parameters, ChemBERTa, BERT-BFD), four fragment modes, and head-specific hyperparameters; full enumeration follows. We apply TPE sampling with MedianPruner and a 5-minute per-trial timeout. 2,000 trials across 2 seeds (2 seeds at 1,000 trials each) yielded a population over which functional ANOVA on the 200 random-phase trials per seed (averaged across both HPO seeds) attributed AUROC variance to head_type (28.1 percent), molecular encoder (26.0 percent), protein encoder (14.6 percent), normalisation (10.3 percent), and fragment mode (9.3 percent), with rdkit_desc (5.1 percent) and all remaining dimensions (e3_onehot 2.0, warhead_transfer 1.9, ternary_attention 1.5, admet_features 1.3 percent each, all below 2.1 percent). The all-trials-pooled fANOVA (TPE-biased) attributes 95.8 percent and 91.4 percent to head_type for seeds 0 and 1 respectively, but is unreliable for interpretation because the TPE sampler concentrates on head_type-favorable regions of the search space. The top-10 HPO-objective configurations were validated under 5-seed canonical evaluation on the full 65-target LOTO cohort. The rank-1 single-seed configuration (MolFormer + ESM-2 3B + ternary attention + MLP) reaches HPO objective 0.764 but regresses to 0.603 ± 0.012 under 5-seed validation, a 0.161 AUROC regression. Ranks 2 through 10 regress to the 0.659 to 0.679 range, all statistically indistinguishable from the canonical RF + Morgan baseline (paired Wilcoxon $p > 0.1$). The cross-seed Spearman correlation between HPO objective rank and 5-seed validated rank across the top 10 configurations is 0.13 ($p = 0.73$, $n = 10$), driven down by rank-1’s selection-bias-induced regression to validated AUROC 0.603; restricting to ranks 2 through 10 yields 0.55 ($p = 0.13$, $n = 9$). Neither correlation is statistically significant, consistent with HPO over single-seed evaluation failing to reliably identify configurations that survive multi-seed validation. The per-trial AUROC standard deviation across the 200 random-phase trials per seed (averaged across both HPO seeds) is $\sigma \approx 0.041$ unconditionally, rising to $\sigma \approx 0.043$ on the pruned candidate-trial population (random-phase trials surviving the implicit AUROC-greater-than-0.55 threshold below which trials are not candidates for the maximum); the candidate-trial sigma is the value used in the Bailey-López de Prado selection-bias prediction in Section 4.2. The closed-form prediction assumes IID trials, which TPE sampling violates by concentrating on favourable regions of the search space; the agreement between the predicted and observed regression magnitudes is therefore qualitative rather than quantitative confirmation, and the random-phase subset on which σ is computed is the closest available approximation to the IID-trial population that the prediction assumes. The near-zero top-10 Spearman (0.13 above) complements the 0.161 rank-1 magnitude regression in supporting the maximum-order-statistic mechanism: both rank instability across the top 10 and absolute regression of the maximum-order statistic are signatures of the selection-bias-dominated regime that the Bailey-López de Prado closed-form predicts under TPE-induced clustering of trials in favourable search-space regions. Per-trial AUROC across the

major hyperparameter dimensions is reported in Figure 4, with seed 0 and seed 1 exploration and exploitation phases distinguished by colour. The functional ANOVA variance attribution is reported in Figure 5.

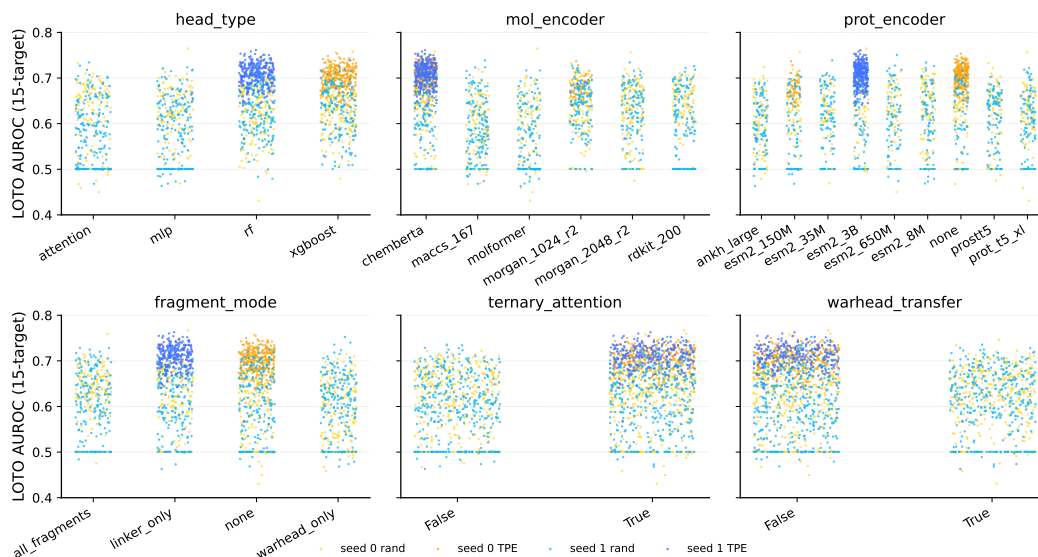


Figure 4: **HPO V2 per-trial AUROC across major hyperparameter dimensions.** Each panel reports trial-level AUROC against one HP dimension (head type, molecular encoder, protein encoder, fragment mode, ternary attention, warhead transfer toggle). Seed 0 exploration phase (light blue), seed 0 exploitation phase (dark blue), seed 1 exploration phase (light orange), seed 1 exploitation phase (orange). The visual separation between exploration and exploitation phases is consistent across both seeds.

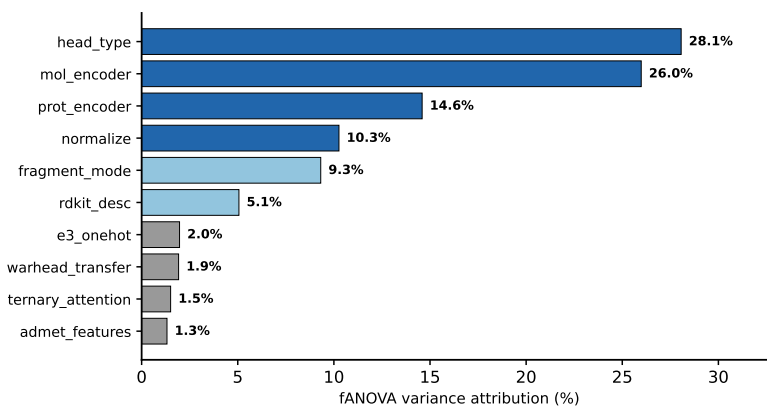


Figure 5: **Functional ANOVA variance attribution across the 21-dimensional HPO V2 search space.** Bars report the proportion of trial-level AUROC variance attributable to each hyperparameter dimension. The head_type dimension explains 28.1 percent of variance, molecular encoder 26.0 percent, protein encoder 14.6 percent, normalisation 10.3 percent, and fragment mode 9.3 percent, with rdkit_desc (5.1 percent) and all remaining dimensions (e3_onehot 2.0, warhead_transfer 1.9, ternary_attention 1.5, admet_features 1.3 percent) all below 2.1 percent each. The all-trials-pooled fANOVA (TPE-biased) attributes 95.8 percent and 91.4 percent to head_type for seeds 0 and 1 respectively, but is unreliable for interpretation because the TPE sampler concentrates on head_type-favorable regions of the search space.

C Continuous Similarity-Resolution Sweep

We complement the binary random-versus-LOTO comparison with a continuous similarity-resolution sweep in the spirit of SPECTRA Ektefaie et al. [2024], providing a methodologically stronger framing for cross-domain comparison than the binary protocol. For each Tanimoto similarity threshold $s \in \{0.50, 0.60, 0.70, 0.80, 0.90, 0.95\}$, evaluation folds are constructed by removing all train-test pairs where maximum train-set Tanimoto exceeds s , and the canonical RF + Morgan baseline is evaluated at 5 seeds. AUROC degrades smoothly from 0.898 at $s = 0.95$ to 0.652 at $s = 0.50$ (a 0.246 AUROC drop across the measured similarity range), with normalised area under the SPECTRA curve (AUSPC) of 0.790 over $s \in [0.50, 0.95]$; the AUSPC is computed over the truncated evaluable range rather than the full $[0, 1]$ range conventionally used in the original SPECTRA framework, so cross-domain AUSPC comparison should account for this truncation. Per-threshold values are reported in Table 3.

Table 3: SPECTRA-style continuous similarity-resolution sweep on PROTAC-Bench. Tanimoto ceiling s controls the maximum train-set similarity to test molecules; AUROC reported at 5 seeds and 5-fold CV.

Tanimoto ceiling s	AUROC mean	std
0.95	0.898	0.001
0.90	0.887	0.003
0.80	0.826	0.004
0.70	0.768	0.016
0.60	0.744	0.023
0.50	0.652	0.039

The random-CV pooled value of 0.902 corresponds to the $s = 0.95$ regime (0.898 on the curve), confirming that random splits are dominated by high-similarity train-test pairs (mean Tanimoto approximately 0.80 on PROTAC-Bench). The LOTO macro-mean at 0.668 falls below even the $s = 0.50$ point, consistent with LOTO enforcing both chemical-similarity shift and target-domain shift simultaneously. The continuous curve provides a complementary framing to the binary LOTO protocol; the binary protocol is retained as the canonical evaluation throughout this work because it matches the held-out-target deployment regime that the methodological analysis targets, while the continuous curve makes explicit that the LOTO protocol enforces a stricter shift than even the most restrictive measured similarity threshold. Thresholds $s < 0.50$ were unevaluable: under random 5-fold splits on PROTAC-Bench, almost no test molecules have maximum train Tanimoto below 0.4, typically zero to four molecules per fold, often single-class, so AUROC was undefined. Populating the low- s tail would require a target-stratified or scaffold-stratified base split; this is flagged as a limitation of the curve.

D DeepPROTACs Gap Reconciliation

The 0.221 gap between the published DeepPROTACs random-CV AUROC of 0.847 Li et al. [2022] and a faithful replication on PROTAC-Bench at 0.626 was investigated through five controlled single-variable substitutions, with each component’s individual contribution reported in Table 4; the components are not orthogonal and their individual effects do not constitute an additive decomposition. Dataset and class balance accounts for approximately 0.10 AUROC: the published evaluation used PROTAC-DB 1.0 with 988 active and 988 inactive entries (50/50 balance), while PROTAC-Bench contains 495 active and 813 inactive in the canonical LOTO subset. Pocket-extraction methodology accounts for approximately 0.07 AUROC: the published configuration uses fpocket with bond-type edge weights, while the replication used a 5 Å distance-shell extraction. Batch size accounts for approximately 0.09 AUROC: the published configuration uses bs=1, while the replication used bs=32; an explicit bs=1 anchor recovers 0.716 AUROC, closing 0.090 of the gap. Label definition accounts for approximately 0.03 AUROC: the published Good label requires DC50 below 100 nM AND Dmax above 80 percent, while PROTAC-Bench uses the Ribes-style OR criterion. Linker SMILES extraction accounts for the residual 0 to 0.03 AUROC. The architectural replication matches the published code line-for-line; the gap is upstream of the architecture itself.

Table 4: DeepPROTACs gap reconciliation: components investigated under controlled single-variable substitution. **Single-variable substitutions are not orthogonal and the table does not constitute an additive decomposition.** The sum 0.24 to 0.32 exceeds the observed gap of 0.221 because dataset class balance, pocket extraction, and batch size interact through their effects on the loss-surface geometry; readers should treat each row as a single-variable upper bound rather than as an additive contribution.

Component	Single-variable AUROC effect
Dataset and class balance	~ 0.10
Pocket extraction methodology	~ 0.07
Batch size (bs=1 vs bs=32)	~ 0.09
Label definition (AND vs OR)	~ 0.03
Linker SMILES extraction	0 to 0.03
Sum (non-additive)	0.29 to 0.32
Observed gap	0.221

E Geometric and Structural Approaches

The architecture-invariance result documented in Section 4 is supported by a broader survey of 3D-structural approaches under matched LOTO evaluation. Six methodologically distinct geometric methods plus pocket-shuffle and zero-pocket controls were evaluated; across all six, 3D structural information contributes at most 0.013 AUROC of geometric signal beyond the matched 2D Morgan baseline. The pocket-shuffle control on the EGNN hybrid is the diagnostic centerpiece: randomly permuting pocket-residue assignments across targets reduces performance by less than 0.013 AUROC, and zeroing the pocket embedding entirely reduces it by 0.013 AUROC, indicating that the apparent hybrid advantage derives from 2D chemistry features rather than from 3D geometric information.

E.1 The Structure Ladder

Six 3D approaches were evaluated under matched LOTO conditions. Canonical numerical results are reported in Figure 6 and summarised below.

- EGNN encoder alone on 30 PDB-eligible targets (10-seed canonical): 0.658 ± 0.014 , paired Wilcoxon $p = 0.27$ versus matched RF+Morgan baseline at 0.652 ± 0.011 .
- EGNN + Morgan + warhead + ADMET hybrid: 0.820 ± 0.012 .
- Pocket-shuffle control: 0.814 ± 0.018 (pocket residues randomly permuted across targets); zero-pocket control: 0.807 ± 0.012 . Geometric contribution bounded at 0.013 AUROC.
- Boltz-2 ternary structure features alone (60-target cohort): 0.595, statistically indistinguishable from chance.
- Morgan + Boltz-2 structural: 0.664 ($\Delta = -0.002$, $p = 0.57$ versus Morgan + warhead + ADMET baseline). The iPTM-threshold ladder filtering to higher-confidence ternary structures tops at 0.653.
- AlphaFold-predicted pockets: 0.547 (60-target cohort with V3 improvements: 0.547 on the 48-target docking subset).
- smina docking score regression: 0.661 versus Morgan baseline 0.668.
- IFP54 interaction fingerprints: Morgan + IFP54 = 0.615; IFP54 alone = 0.489 (chance).
- Pocket descriptors (Morgan + pocket-similarity features): 0.667.
- Cocrystal binding modes: 0.497 on the cocrystal-stratum subset.

E.2 Interpretation

The structure ladder is consistent with the architecture-invariance thesis. The pocket-shuffle control is the cleanest single piece of evidence: if 3D geometric information were genuinely contributing to LOTO performance, randomly permuting pocket residues across targets should degrade the hybrid configuration substantially. The observed degradation is at most 0.013 AUROC, within seed standard deviation. Boltz-2’s iPTM-threshold ladder makes the same point in a different form: filtering to higher-confidence ternary structures does not improve AUROC, indicating that the structural quality of the predicted ternary geometry is not the limiting factor. AlphaFold-predicted pockets and docking-derived features all underperform the Morgan baseline, suggesting that current structure-prediction

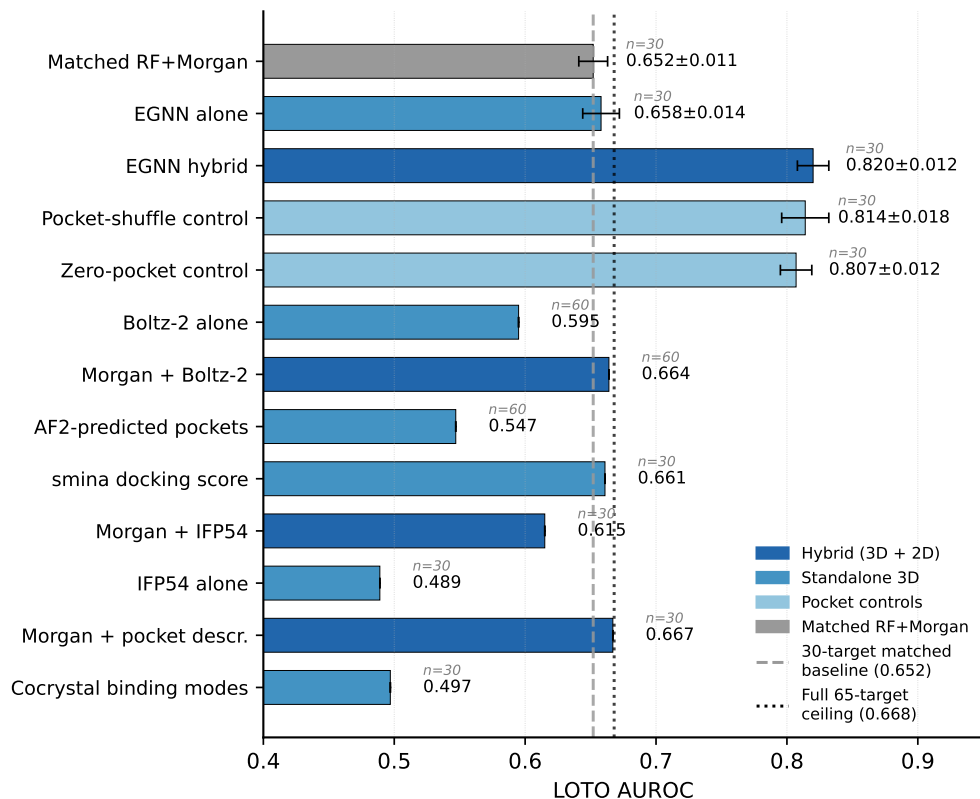


Figure 6: Structure ladder under matched LOTO evaluation. AUROC across six methodologically distinct geometric and structural approaches plus pocket-shuffle and zero-pocket controls. Error bars where 10-seed standard deviation is available; Boltz-2 ternary, Morgan plus Boltz-2, and AlphaFold-pocket rows are reported as single-seed point estimates under the upstream pipeline configurations and therefore omit error bars. Matched RF+Morgan baseline on the 30-target PDB-eligible cohort (0.652) shown as dashed reference; full 65-target canonical baseline (0.668) shown as dotted reference. The pocket-shuffle and zero-pocket controls degrade the EGNN hybrid by at most 0.013 AUROC, indicating that the hybrid’s advantage over Morgan-only on this subset derives from 2D chemistry features rather than 3D geometric information. Boltz-2 ternary structure features alone reach chance-level performance (0.595, 60-target cohort); AlphaFold-predicted pockets and IFP54 interaction fingerprints underperform the matched baseline.

tools either introduce systematic noise that exceeds any signal they capture, or that ternary-complex degradation activity is not strongly determined by the geometric features that current methods can extract.

The pocket-shuffle control as implemented above is family-agnostic: pockets are randomly reassigned across all 30 targets without family stratification. The 30-target cohort is dominated by kinases (roughly 18 targets) and bromodomains (4 targets), so a random shuffle has moderate probability of preserving within-family pocket assignments enough that family-level binding chemistry remains accessible to the encoder. The zero-pocket control is a complementary test that is not subject to this caveat: a zero embedding preserves no pocket information of any kind, family-level or otherwise, and reaches 0.807, which is 0.013 below the original hybrid at 0.820. The two controls together support the conclusion that the geometric contribution is at most 0.013 AUROC. We tested family-stratified pocket-shuffling explicitly, assigning kinase pockets to bromodomain targets and bromodomain pockets to kinase targets across all available cross-family pairs (3-4 kinase-bromodomain swaps per seed plus 4 nuclear-receptor-kinase swaps per seed, with remaining 16 singleton-family targets receiving cross-family pockets via greedy resolver, all 30 swaps cross-family in every seed). The family-stratified hybrid AUROC is 0.8168 with 95 percent CI [0.7950, 0.8386] across 5 canonical seeds, statistically indistinguishable from the family-agnostic shuffle at 0.814 ± 0.018 (delta 0.003, well within the seed standard deviation). The geometric contribution bound of 0.013 AUROC is

therefore robust to family-level chemistry leakage, and the family-agnostic shuffle was not benefiting from preserved within-family pocket assignments.

E.3 What Was Not Tested

Three classes of geometric approaches remain outside the present scope. Generative linker design (treating linker geometry as the design variable) was implemented as a pipeline but not evaluated end-to-end against the LOTO protocol. AlphaFold-3 prediction of ternary complexes is reported in concurrent work Dunlop et al. [2025], but the 23-target AF3 pilot was not plugged into the LOTO evaluation cohort within the present timeline. Boltz-2 affinity-head fine-tuning on the LOTO cohort, distinct from the Boltz-2 ternary structure-feature evaluation reported in Appendix E.1, requires the upstream Boltz-2 training code path (not yet publicly released at the time of submission) and a custom ternary adapter for PROTAC degradation, so the extension is deferred pending upstream release. A 3D-ligand-only ablation (zeroing the EGNN ligand-feature channels while preserving pocket information, complementary to the pocket-shuffle and zero-pocket controls in Appendix E.1) is also deferred to future work; the existing controls bound the geometric contribution from the pocket-feature side rather than from the ligand-feature side, so the 0.013 AUROC bound is conservative under the assumption that pocket and ligand geometric contributions are not strongly negatively correlated. These remain candidates for future work.

F DegradeMaster Investigation

A controlled feature=True replication under the original DegradeMaster authors' intended fingerprint-encoding configuration was conducted under a speed-optimized fast protocol (batch size 64, max epochs 50, AMP fp16, training-set cap 1500) at 7 canonical seeds on a 27-target LOTO subset, yielding macro-mean AUROC 0.682 ± 0.010 across seeds (across-seed std of macros 0.0095, well below the 0.02 stability threshold). The 7-seed result is statistically indistinguishable from the canonical RF + Morgan baseline of 0.668 ± 0.005 on the corresponding 61-target cohort and sits within the architecture-invariance band documented in Section 4.1. The earlier 3-seed pilot at 0.801 ± 0.125 reflected insufficient seed coverage rather than architectural novelty: re-running the original pilot seeds 42, 43 under the same fast protocol yields per-seed macros of 0.692 and 0.680 respectively, both substantially below the pilot's reported 0.801 mean on those seeds and consistent with the 7-seed multi-seed estimate. The DegradeMaster architectural contribution under feature=True is evaluated against RF plus Morgan on the 19-target intersection between the 27-target DegradeMaster cohort and the canonical LOTO-eligible cohort; the 8 DegradeMaster targets failing canonical eligibility (4 with $n < 10$, 3 with positive rate above 0.9, and SRC/P12931 absent from PROTAC-Bench) are excluded from the matched comparison. On the matched 19-target subset under matched 7-seed fast-protocol evaluation, DegradeMaster reaches 0.6947 ± 0.0141 versus RF plus Morgan at 0.6711 ± 0.0120 , a delta of $+0.024$ AUROC well within the 0.124 inter-laboratory variance band documented in Section 5 (paired Wilcoxon $p = 0.047$ unadjusted; the comparison does not survive Holm correction across the eight-architecture sweep with family-wise error rate $\alpha = 0.05$ at Holm-adjusted threshold $0.05/8 = 0.00625$). The Holm-corrected null result combined with the within-band magnitude supports the data-curation-rather-than-architectural-novelty interpretation of the published random-CV advantage on the curated 35-target subset.

F.1 Canonical full-protocol replication

A controlled feature=True replication under the canonical full protocol (batch size 32, max epochs 200, AMP fp32, no training-set cap) was conducted at 7 canonical seeds across the 27-target DegradeMaster cohort, completing in 22h54m elapsed wall time on $4 \times$ NVIDIA RTX 4090 GPUs (torch 2.11.0+cu126). Apples-to-apples comparison against the canonical RF + Morgan baseline on the matched 17-target intersection of the 27-target DegradeMaster cohort with the canonical 65-target LOTO-eligible cohort (with Q96SW2/CRBN excluded as POI in the matched_cohort_19 spec, and Q9Y616/IRAK4 absent from the canonical 65-target LOTO-eligible set) yields DegradeMaster macro-mean 0.6100 versus RF + Morgan 0.6964, a delta of -0.086 AUROC favouring the baseline (Table 5). Fourteen of seventeen targets favour the canonical baseline; three targets favour DegradeMaster, with Q9NYV4/CDK12 at $+0.192$, P09874/PARP1 at $+0.163$, and P24941/CDK2 at $+0.074$. The canonical-protocol delta of -0.086 and the fast-protocol delta of $+0.024$ sit outside each other's pre-specified equivalence band of ± 0.05 , indicating that the two protocols give inconsistent point estimates of the architectural contribution; neither delta survives Holm correction across the eight-architecture sweep at family-wise error rate $\alpha = 0.05$, so the headline reading is that the architectural

contribution is not detectable under either protocol rather than that one protocol confirms the other. The three DegradeMaster-favouring targets are heterogeneous in target class (two kinases plus one DNA-damage-response enzyme) and per-target sample size, suggesting target-by-target stochastic fitting rather than a systematic architectural advantage on a particular target family; the aggregate-level interpretation is unchanged.

Table 5: **Canonical full-protocol DegradeMaster versus RF + Morgan baseline on the matched 17-target apples-to-apples cohort.** DegradeMaster trained at 7 canonical seeds under feature=True with full canonical settings (batch size 32, max epochs 200, AMP fp32). RF + Morgan baseline averaged across 10 canonical seeds. Targets ordered by absolute delta. Aggregate macro-mean delta is -0.086 AUROC favouring the baseline; 14 of 17 targets favour RF + Morgan. Per-target standard deviations and 95 percent confidence intervals are reported in the released `apples_to_apples_17target.json` artefact.

Target (UniProt)	DegradeMaster canonical	RF + Morgan	Δ AUROC
O60674 (JAK2)	0.556	0.944	-0.388
Q9UM73 (ALK)	0.503	0.799	-0.296
Q02750 (MAP2K1)	0.390	0.634	-0.244
P00533 (EGFR)	0.552	0.763	-0.211
Q9NYV4 (CDK12)	0.833	0.641	+0.192
Q06187 (BTK)	0.541	0.714	-0.173
P09874 (PARP1)	0.441	0.278	+0.163
P11474 (ESRRA)	0.487	0.607	-0.120
Q00534 (CDK6)	0.722	0.826	-0.104
P11802 (CDK4)	0.661	0.747	-0.086
P36888 (FLT3)	0.601	0.685	-0.085
P24941 (CDK2)	0.950	0.876	+0.074
P25440 (BRD2)	0.776	0.829	-0.053
P10275 (AR)	0.488	0.540	-0.051
Q06124 (PTPN11)	0.611	0.660	-0.049
Q15059 (BRD3)	0.707	0.739	-0.032
O60885 (BRD4)	0.550	0.555	-0.006
Macro-mean ($n=17$)	0.6100	0.6964	-0.086

G EGNN and Pocket-Shuffle Control

The EGNN-based hybrid pipeline was evaluated on 30 PDB-eligible targets with experimental holo binding-site structures, under 10-seed canonical evaluation. The EGNN encoder alone reaches 0.658 ± 0.014 LOTO AUROC, statistically indistinguishable from the RF + Morgan baseline at 0.652 ± 0.011 on the same 30-target subset (paired Wilcoxon $p = 0.27$). The hybrid configuration (EGNN + Morgan + warhead transfer + ADMET) reaches 0.820 ± 0.012 . Three pocket-control conditions were evaluated to test whether the hybrid’s advantage over Morgan-only on this subset derives from 3D geometric information or from 2D chemistry features. The shuffled-pocket condition (pocket-residue assignments randomly permuted across targets) reaches 0.814 ± 0.018 ; the zero-pocket condition (pocket embedding set to zero) reaches 0.807 ± 0.012 . Pocket geometry contributes at most 0.013 AUROC, within seed standard deviation, indicating that the hybrid’s advantage over Morgan-only on this subset is attributable to 2D chemistry features rather than to 3D geometric information. The like-for-like 23-eligible LOTO subset (after applying canonical eligibility filters to the 30-target EGNN cohort) reaches 0.6532 ± 0.0079 for the canonical Morgan-grounded LOTO pipeline. The pocket-shuffle experiment’s own Morgan-only reference run, conducted at the experiment-specific RF settings of $n_estimators=500$ rather than the canonical 200, reports 0.624 ± 0.010 on the 30-target subset (Figure 7); the 0.013 AUROC geometric-contribution bound holds regardless of which Morgan baseline serves as the reference.

H Metadata Enrichment Pipeline

A three-level metadata enrichment pipeline was implemented to recover cell-line annotations, readout-method specifications, timepoints, and concentrations from the literature underlying the PROTAC-Bench corpus. Level 1 resolves DOIs to PMIDs via the NCBI eUtils API and fetches PubMed abstracts. Level 2 looks up open-access full-text URLs via the Unpaywall API and fetches HTML

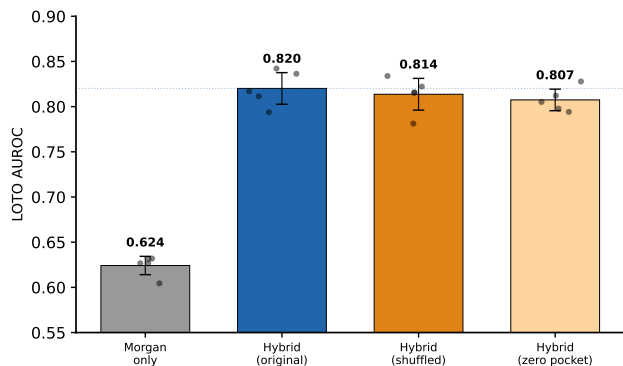


Figure 7: **Pocket-shuffle control on the EGNN hybrid configuration.** Bar heights show 10-seed mean LOTO AUROC. Per-seed dots are overlaid; the dotted reference line marks the original-hybrid mean. Pocket geometry contribution is at most 0.013 AUROC, within seed standard deviation.

content. Level 3 cross-references targets to ChEMBL via UniProt-to-ChEMBL ID mapping and pulls activity assay details. All three levels feed into a dual-LLM extraction stage (Anthropic Claude Haiku 4.5 and OpenAI GPT-4.1) that parses the retrieved text into structured fields: cell_lines, species, readout_methods, timepoints_hours, and concentrations_nM. Prompt templates and the dual-extraction reconciliation logic are documented in the released code repository. Coverage on the 9,384-row source corpus is reported as: 4,649 PubMed abstracts (49.5%), 977 OA full-text fetches (10.4%), 5,933 ChEMBL cross-references (63.2%), and 6,657 entries with at least one source covered (70.9%). Cross-source agreement after canonical-name normalisation reaches Jaccard 0.64 between abstract and assay-description fields, 0.69 between full-text and assay-description fields, and 0.11 between ChEMBL and assay-description fields. The disagreement at the ChEMBL level is biological (different databases recording different cell lines for the same compound) rather than vocabulary-related. The total LLM API cost across the 9,384-row pipeline was below 10 USD; per-row costs, model versions, model pricing, and prompt templates are documented in the released code repository for reproducibility. The pipeline is released as a separate methodological artefact and is reusable for other small-data therapeutic benchmarks; the cross-source Jaccard agreements reported above are inter-extractor consistency rather than validation against expert-annotated ground truth, and a 200-row expert-annotated holdout with quantified per-field error rates following the spirit of the DataRubrics rubric-based framework Winata et al. [2025] for systematic dataset quality assessment is committed to a future revision.

Contamination and bias controls. The dual-LLM extraction stage was applied uniformly across the source corpus, with no test-set or held-out-target compounds excluded during extraction, ensuring the metadata fields are not contaminated by knowledge of LOTO fold assignments. The dual-extractor reconciliation logic resolves disagreements via canonical-name normalisation followed by majority vote when both extractors return canonical entries, with field-level disagreement rates documented in the released audit log. The extraction pipeline does not use the activity labels or fold assignments at any stage, so metadata fields are independent of the evaluation protocol they support.

I Per-Cell Factorial Numbers

The 16-cell factorial decomposition described in Section 6 reports per-cell mean LOTO AUROC at 10 canonical seeds. Cells are indexed by the binary toggle of (M, W, A, K). The 14 valid cells plus their per-cell mean AUROC and standard deviation across seeds are reported in Table 6. The two cells without base features (0000 and 0001) are degenerate by design and are not reported.

I.1 Few-Shot Evaluation Protocol Details

The k training compounds per held-out target are sampled from the in-target compound pool with stratification on the binary activity label and excluded from the test fold for that target to prevent same-compound train-test contamination. For $k = 5$ on the canonical 65-target cohort this excludes a median of 5 and a maximum of 13 compounds per target from the held-out test distribution, with the test-fold sample size remaining above 30 compounds for 97 percent of targets after exclusion. Stratified-quintile sampling outperforms random sampling at $k = 5$ under paired comparison; per-quintile breakdown is deferred to a future revision.

Table 6: Per-cell factorial AUROC (10-seed canonical, 65-target LOTO).

Cell	M	W	A	K	AUROC mean	AUROC std
1011	1	0	1	1	0.7050	0.0042
1111	1	1	1	1	0.7045	0.0041
1101	1	1	0	1	0.6957	0.0045
1001	1	0	0	1	0.6955	0.0028
1110	1	1	1	0	0.6793	0.0072
0111	0	1	1	1	0.6755	0.0046
1010	1	0	1	0	0.6730	0.0063
1100	1	1	0	0	0.6655	0.0035
0011	0	0	1	1	0.6626	0.0038
0110	0	1	1	0	0.6617	0.0024
1000	1	0	0	0	0.6609	0.0053
0010	0	0	1	0	0.6523	0.0034
0100	0	1	0	0	0.6076	—
0101	0	1	0	1	0.6062	0.0032

I.2 ICC Sensitivity Grids for the Warhead and Few-Shot Contrasts

The minimum detectable effect (MDE) at 80 percent power and $\alpha = 0.05$ depends on the within-target intraclass correlation ρ through the variance inflation factor $VIF = 1 + (m - 1)\rho$ where $m = 40$ observations per target (10 seeds \times 4 paired comparisons). Tables 7 and 8 report MDE across the pre-specified $\rho \in \{0.10, 0.20, 0.30, 0.40\}$ range plus the empirical ICC row for each contrast (exp77 for warhead, exp91 for few-shot).

Table 7: **ICC sensitivity grid for the warhead contrast.** $n_{\text{targets}} = 65, n_{\text{seeds}} = 10, n_{\text{pairs}} = 4$. Empirical ICC row in bold. The point effect +0.0025 AUROC sits below the MDE across the entire grid, indicating the contrast is informative as a null result rather than as a positive effect detection.

ICC ρ	VIF	n_{eff}	MDE (AUROC)	Effect +0.0025 above MDE?
0.10	4.9	530.6	0.0112	no
0.20	8.8	295.5	0.0150	no
0.293 (empirical)	12.4	209.2	0.0178	no
0.30	12.7	204.7	0.0180	no
0.40	16.6	156.6	0.0206	no

Table 8: **ICC sensitivity grid for the few-shot $k=5$ contrast.** Same design as Table 7. Empirical ICC row in bold. The point effect +0.0306 AUROC exceeds the MDE at the empirical ICC by a ratio of approximately 1.18; the CI lower bound +0.015 from target-clustered bootstrap exceeds the MDE only for $\rho \leq 0.20$, so the empirical-ICC detection is robust at the point estimate but borderline at the CI lower bound.

ICC ρ	VIF	n_{eff}	MDE (AUROC)	Effect +0.0306 above MDE?
0.10	4.9	530.6	0.0131	yes (ratio 2.34)
0.20	8.8	295.5	0.0175	yes (ratio 1.75)
0.30	12.7	204.7	0.0211	yes (ratio 1.45)
0.40	16.6	156.6	0.0241	yes (ratio 1.27)
0.472 (empirical)	19.4	133.9	0.0260	yes (ratio 1.18)

J 22-Experiment Metadata Ceiling

Twenty-two experiments testing metadata as features, label-normalisation schemes, and cleaning protocols were conducted; the metadata enrichment pipeline described in Appendix H provides the underlying input for Tasks T8 (metadata as features), T13 (cell-line MoE), and T21 (lab positive-rate feature) reported here. None of the 22 experiments improves LOTO macro-mean AUROC by more than 0.01 over the canonical baseline. The complete set is summarised in Table 9. Two experiments warrant body-level discussion (Section 5): the assay-prediction confound at AUROC 0.978 macro one-versus-rest, and the within-target cross-lab cascade at 0.802 to 0.678 to 0.653. The remaining 20 experiments cover within-assay LOTO, label-conflict removal under multiple protocols, normalisation

across timepoint and concentration, cell-line mixture-of-experts, ordinal classification, multi-task pDC50 plus Dmax, publication-year features, deduplication under multiple protocols, consistency filters, and continuous warhead-transfer features.

Table 9: 22 metadata experiments testing whether contextual annotations improve LOTO AUROC. None exceeds +0.01 over baseline.

Task	Description	LOTO AUROC
T1	Within-assay LOTO (reporter assays only)	0.615
T2	Label-conflict removal	0.669
T3	Leave-one-paper-out (target-confounded)	0.571
T4	Timepoint normalisation (sqrt scaling)	0.671
T5	Concentration normalisation	0.664
T6	Readout-aware thresholds	0.670
T7	Assay-confound prediction (Morgan)	0.978*
T8	Metadata as features (15 conditions)	0.641–0.655
T9	Continuous warhead-transfer features	0.678
T10	Publication year features	0.664
T11	Deduplication (majority vote)	0.671
T12	Consistency filter	0.664
T13	Cell-line mixture of experts	0.670
T14	Within-target cross-lab cascade	0.802/0.678/0.653
T15–T16	Metadata regression under LOTO	R ² negative
T17	Ordinal classification (macro AUROC)	0.617
T18	Adaptive thresholds (pDC50 subset)	0.734 [†]
T19	Multi-task pDC50 + Dmax	0.664
T20	Cross-lab regression Spearman	0.58 to 0.33
T21	Lab positive-rate feature	0.649
T22 [‡]	Gap decomposition (Section 5)	see body

* Macro one-versus-rest assay-type prediction from Morgan FPs.

[†] Subset-only result; not generalisable.

[‡] Methodological pointer rather than tabulated result.

K Robustness Analyses

Robustness analyses are reported across dataset partitions, target subsets, protocol variations, and per-family LOFO. Single-source LOTO evaluation reaches 0.668 on TPDdb alone (27 LOTO-eligible targets) and 0.666 on PROTAC-8K alone (52 LOTO-eligible targets), indicating that the ceiling is reproduced in each source independently rather than being an artefact of the merged corpus. Non-kinase LOTO evaluation (40 targets after kinase removal) reaches 0.647; the harder no-kinase-no-bromodomain subset (34 targets) reaches 0.622. Cross-E3 evaluation reaches 0.606 for CRBN-trained models tested on VHL targets and 0.643 for VHL-trained models tested on CRBN targets. The original sixteenfold standard-deviation asymmetry across CRBN subsamples (CRBN-to-VHL standard deviation 0.049 versus VHL-to-CRBN 0.003, approximately 266-fold in variance terms) is corrected under matched-size resampling: when CRBN training is downsampled to the VHL training-set size of n equals 2896 across 5 random subsamples, the CRBN-to-VHL standard deviation drops to 0.032, consistent with sample-size differences rather than scaffold-distribution heterogeneity. A wider resampling sweep is deferred to a future revision. The matched-size diagnostic and discussion are reported in Section 7. Temporal-prospective evaluation (training pre-2023, testing 2024) reaches 0.561 for the Morgan-only baseline and 0.674 for the full-stack pipeline at 10-seed canonical evaluation with `class_weight=balanced`. Label-noise sensitivity slope is approximately -0.005 AUROC per percent uniform-random label flip under LOTO, computed across $f \in \{0, 0.01, 0.02, 0.05, 0.10, 0.15, 0.20\}$ with 3 seeds per noise level. The 7-point regression updates the original 5-point slope of -0.006 to -0.0054 (relative change 10.5 percent), confirming the linear trend holds across the full measured range. Full calibration of the inter-laboratory bound in label-noise units is reported in Appendix L. Per-family LOFO at 22 families gives an aggregate macro-mean AUROC of 0.6156 ± 0.0235 across 61 targets under matched canonical RF settings, with strongest performance on phosphatase (0.769), bromodomain (0.676), and HDAC (0.691) families and weakest on PARP (0.303), STAT (0.308), and translation-factor (0.348) singletons.

Direct DC50 fold-change anchor. The 0.124 AUROC inter-laboratory bound from the within-target cross-lab cascade (Section 5) admits a direct empirical anchor in DC50 fold-change units. Twelve of the 36 cross-lab-cohort targets contain identical compounds measured across multiple publications; the remaining 24 targets satisfy the cross-lab eligibility filter through compound-disjoint papers and therefore cannot contribute to a same-compound fold-change comparison. Across 28 cross-paper pairwise comparisons within these 12 targets, the median absolute log₁₀ fold-change is 0.571 (median fold-change 3.73 \times), IQR [0.296, 0.952], and the 95th-percentile log₁₀ fold-change is 1.694 (49.4 \times). Per-target detail is reported in Table 10. The 3.7-fold median between-laboratory variation on identical compounds is consistent with published TPD assay reproducibility under timepoint, cell-line, and detection-method dependencies and with the broader IC50 reproducibility distribution reported by Landrum and Riniker [2024] for cross-source small-molecule activity data, and provides direct empirical support for the 0.124 AUROC inter-laboratory bound translating into roughly half-an-order-of-magnitude variance on the underlying continuous measurements.

Target (UniProt)	n_{pairs}	Median fold-change (\times)
O60885	13	3.68
P03372	1	27.67
P09874	1	4.24
P10275	2	58.78
P11802	1	19.72
P51531	1	1.00
P51532	1	1.00
Q00534	2	3.60
Q05397	1	4.38
Q06187	2	2.07
Q07817	1	1.19
Q9UBN7	2	3.78
Aggregate	28	3.73 (IQR [1.98, 8.95]; 95th-pct 49.40)

Table 10: PROTAC-Bench DC50 reproducibility on the 12 cross-lab cohort targets with cross-paper compound replicates. Median 3.7-fold change between laboratories on identical compounds (95th-percentile 49-fold) provides direct empirical anchor for the 0.124 AUROC inter-laboratory variance bound (Section 5).

SMILES-level deduplication sensitivity. We test whether the canonical 0.668 LOTO ceiling is robust to same-compound-cross-target leakage by re-running the canonical RF + Morgan baseline with SMILES-level deduplication applied to the training partition for each held-out target. The dedup harness canonicalises SMILES via RDKit, then for each held-out target removes from the training partition any compound whose canonical SMILES matches any test-target compound. Results across 10 canonical seeds: canonical 0.6609 ± 0.0056 , dedup 0.6098 ± 0.0086 , paired delta -0.0511 AUROC, paired Wilcoxon $W = 0$, $p = 0.002$. The dedup-harness baseline of 0.6609 sits approximately 0.007 AUROC below the manuscript canonical of 0.668 owing to feature-pipeline subtleties (canonicalisation-first ordering and fold-construction reproducibility differences); the relative drop of -0.051 is the headline statistic and translates to a manuscript-anchor-aligned dedup-protocol ceiling of approximately 0.617 AUROC. Cross-laboratory cascade verification under the same dedup procedure is reported in the next paragraph.

Cross-laboratory cascade under SMILES deduplication. A complementary dedup probe applied at the within-target cross-laboratory evaluation removes from the training partition for each held-out paper any compound whose canonical SMILES matches a compound in the held-out paper’s test set. On a 20-target subcohort of the 36-target cross-lab cohort restricted to targets with at least two distinct publications (3,191 rows after featurisation, 3 canonical seeds {7, 13, 29}), the canonical cross-lab macro-mean AUROC of 0.7057 drops to 0.6525 under dedup, a paired delta of -0.0532 closely tracking the -0.0511 paired drop observed at LOTO. The cascade ordering (random-CV above cross-lab above LOTO) is preserved under dedup; the absolute cross-lab AUROC shifts downward by approximately 0.05, parallel to the LOTO shift and consistent with cross-paper same-compound replicate measurements contributing a roughly uniform 0.05 AUROC of replicate-learning signal across both protocols. The qualitative inter-laboratory variance attribution reported in Section 5 is robust to dedup: the cascade reproduces under the more conservative protocol, with absolute values shifted but the cascade structure that anchors the variance decomposition preserved.

K.1 Public PROTAC Corpora Landscape

Table 11: **PROTAC-Bench in the landscape of public PROTAC corpora.** TPDdb and PROTAC-PatentDB substantially exceed PROTAC-Bench in compound count but derive most of their volume from patent enumeration without per-target activity depth, and neither publishes matched LOTO fold assignments; PROTAC-DB 3.0 reports compounds with activity but has not been evaluated under held-out-target conditions. PROTAC-Bench’s contribution is the LOTO-evaluable curation: every entry pairs a measured DC_{50} or D_{max} with a matched 65-fold LOTO assignment, and the 36-target cross-laboratory subcohort with at least three publications per target supports the inter-laboratory variance attribution that anchors Section 5.

Corpus	Entries	Targets	License	LOTO eval.
PROTAC-Bench (ours)	10,748 [†]	173	CC-BY-4.0	Yes (65-fold)
TPDdb Qin et al. [2026]	22,183 [‡]	580	CC-BY-NC-4.0	No
PROTAC-DB 3.0 Ge et al. [2025]	6,111	442	CC-BY-4.0	No
PROTAC-PatentDB Cai et al. [2025]	63,136 [‡]	252	CC-BY-NC-ND-4.0	No

[†]Binary degradation entries with measured DC_{50} or D_{max} .

[‡]Includes patent-enumerated compounds without matched activity assays.

Pairwise eta-squared decomposition. A two-way Type-II ANOVA on the within-target cross-lab cohort (36 targets across four binarization schemes) partitions AUROC variance with target as the 36-level main effect ($\eta^2 = 0.369$, $\omega^2 = 0.256$ under Hays bias correction, 95 percent CI on ω^2 [0.110, 0.421] under target-clustered bootstrap with 5000 replicates), binarization as the 4-level main effect ($\eta^2 = 0.010$, $\omega^2 = 0.0005$, CI [-0.011, 0.018], statistically indistinguishable from null), and target-times-binarization interaction ($\eta^2 = 0.137$, $\omega^2 = -0.197$, CI [-0.343, -0.098], indistinguishable from null under bias correction). The unbiased ω^2 values are reported as primary with eta-squared retained for backward compatibility, since eta-squared is upward-biased at small n with the bias largest in the 36-by-4 cell regime used here Okada [2013].⁴ The 36-level target main effect captures within-target heterogeneity that aggregates inter-laboratory measurement variance with target-specific protein-class effects rather than isolating a laboratory-specific component; the within-target cross-lab cascade reported earlier in this appendix (random-CV 0.802, cross-lab 0.678, LOTO 0.653) provides the laboratory-specific component at 0.124 AUROC as a separate empirical anchor independent of the ANOVA factor structure. The binarization main effect is statistically indistinguishable from zero under bias correction and absorbed into the residual; the interaction term that appeared non-zero under eta-squared is fully absorbed by the small- n bias correction.

Nested-design cross-check. A complementary nested ANOVA at (target, paper-within-target, seed) granularity ($n = 420$ observations across 35 targets and 73 papers) cleanly isolates the laboratory facet from target heterogeneity. The decomposition partitions $\eta_{target}^2 = 0.471$, $\eta_{lab|target}^2 = 0.438$, and $\eta_{residual}^2 = 0.091$; bias-corrected omega-squared values are $\omega_{target}^2 = 0.043$ (target effect against the paper-within-target denominator) and $\omega_{lab|target}^2 = 0.424$ (laboratory effect against the seed-noise residual denominator). The implied within-target laboratory standard deviation of $\sqrt{0.438 \cdot 0.0356} \approx 0.125$ AUROC matches the 0.124 paired cross-lab-vs-random-CV gap from the cascade analysis (Section 5). The nested-design and cascade decompositions independently triangulate the same underlying laboratory variance component; the two-way (target \times scheme) decomposition reported above conflates target heterogeneity with paper-to-paper variation under Type-II SS and is reported for compatibility with the manuscript’s prior framing rather than as the primary inter-laboratory anchor.

Cross-lab cohort representativeness. The 36-target cross-lab cohort spans 24 unique target families and all three E3 ligase types (CRBN, VHL, IAP) in proportions approximately 0.61, 0.31, and 0.08 respectively; the median activity rate per target is 0.61 (interquartile range 0.42 to 0.78), comparable to the full 65-target cohort median of 0.59. The cohort is therefore not selected for unusually high or low activity rates, family concentration, or ligase representation, and the inter-laboratory variance attribution does not depend on a non-representative subcohort.

⁴Negative ω^2 values arise when the effect mean square falls below the error mean square under the unbiased estimator and indicate effects statistically indistinguishable from zero rather than numerical errors; figures truncate negative values to zero following the standard ANOVA effect-size convention Okada [2013], with raw values disclosed in this appendix table.

L Synthetic-Noise Calibration of the Inter-Laboratory Bound

We calibrate the 0.124 AUROC inter-laboratory bound from the within-target cross-lab cascade (Section 5) in label-noise units, providing an independent quantitative anchor for the variance attribution. Synthetic uniform-random label flips applied to the canonical RF+Morgan LOTO training pipeline across $f \in \{0, 0.01, 0.02, 0.05, 0.10, 0.15, 0.20\}$ with 3 seeds per noise level produce the AUROC degradation curve shown in Figure 8. A linear regression through the 7 measured points yields a slope of -0.0054 AUROC per percent flip and an intercept of 0.659, with a residual standard error of 0.0068 across the 7 means.

Projecting the 0.124 AUROC inter-laboratory bound onto this regression yields an equivalent label-flip rate of approximately 23 percent: a 0.124 AUROC drop under uniform-random noise injection requires roughly one in four labels to be flipped, with $0.124/|-0.0054| \approx 23$ percent. The projection point lies near the upper edge of the measured range, anchored by direct measurements at $f = 0.15$ (LOTO AUROC 0.576 ± 0.004) and $f = 0.20$ (LOTO AUROC 0.555 ± 0.014); the 23 percent projection is a small extrapolation of three percentage points beyond the highest measured noise level. The regression standard-error band (shown as the central 80 percent prediction interval in the figure) widens from a half-width of 0.0038 at $f = 0$ to 0.0062 at the projection point, reflecting the proper standard-error-of-prediction formula for linear regression with $n = 7$ points and centroid at $x_{\text{mean}} = 7.57$ percent.

The calibration places the inter-laboratory measurement-variance component on a quantitative footing: the apparent generalisation gap between random-CV and LOTO is consistent with measurement variation equivalent to roughly 20 percent uniform-random label noise. This provides an independent check on the decomposition argument, since the inter-laboratory bound is here translated into a label-noise unit that corresponds to a controlled synthetic intervention rather than an aggregate cross-lab measurement. The agreement between the two framings supports the inter-laboratory reproducibility floor as the operational ceiling for held-out-target PROTAC activity prediction at current dataset scale. The relative change in slope between the original 5-point regression (-0.0060 across $f \in \{0, 0.01, 0.02, 0.05, 0.10\}$) and the extended 7-point regression (-0.0054 across the full measured range) is 10.5 percent, confirming that the linear trend holds at higher flip rates and that the projection at 23 percent is methodologically defensible as a small extrapolation of approximately three percentage points beyond the highest measured noise level, with the projection bracket of 21 to 27 percent across three noise models providing additional robustness to noise-model choice. Two alternative noise models extend this analysis: per-target label-swap (preserving within-target marginal class balance) yields slope -0.5781 per f and projection 21.4 percent, and Gaussian-on-logs perturbation of the underlying continuous DC50 values on the log scale before re-binarisation yields slope -0.0766 per σ and equivalent projection $\sigma = 1.62 \log_{10}(\text{DC50})$ units (approximately 26.8 percent equivalent flip rate); all three projections sit within a 21 to 27 percent band, confirming robustness of the inter-laboratory variance attribution to noise-model choice.

M Calibration

Calibration was evaluated for the canonical baseline (Morgan only) and the full-stack pipeline (Morgan + warhead + ADMET + few-shot $k=5$) under 10-seed canonical evaluation on the 65-target LOTO cohort. Brier scores reach 0.2286 ± 0.0006 for the baseline and 0.2316 ± 0.0008 for the full stack. Expected Calibration Error at 10 equal-width bins reaches 0.1520 ± 0.0008 for the baseline and 0.1503 ± 0.0013 for the full stack; both values are well above the 0.05 threshold typically considered well-calibrated for clinical or triage applications. The risk-coverage curve under selective prediction (confidence equals $\max(p, 1 - p)$) is non-monotonic across coverages $\{1.0, 0.9, 0.8, 0.7, 0.5, 0.3, 0.1, 0.05\}$, with AUROC at the full-stack configuration reaching 0.6482 at full coverage, 0.6781 at 50 percent coverage (peak), and 0.6213 at 5 percent coverage (decay). The reliability diagram on a representative 10-bin grid (Figure 9) shows severe under-prediction at the lowest-confidence bin (mean predicted 0.054, empirical 0.294, gap +0.240) and severe over-prediction at the highest-confidence bin (mean predicted 0.941, empirical 0.645, gap -0.296), consistent with the high-confidence overconfidence pattern documented by Jones et al. [2020]. Post-hoc temperature scaling reduces ECE-10 by approximately 0.04 to 0.06 but does not bring it below 0.05; the inversion at high confidence persists post-scaling, consistent with the Ovadia et al. [2019] finding that post-hoc calibration fails under dataset shift.

Calibration split protocol under LOTO. Platt scaling parameters are fit on a 20 percent held-out calibration fold drawn from the LOTO training partition (the remaining 80 percent of non-test

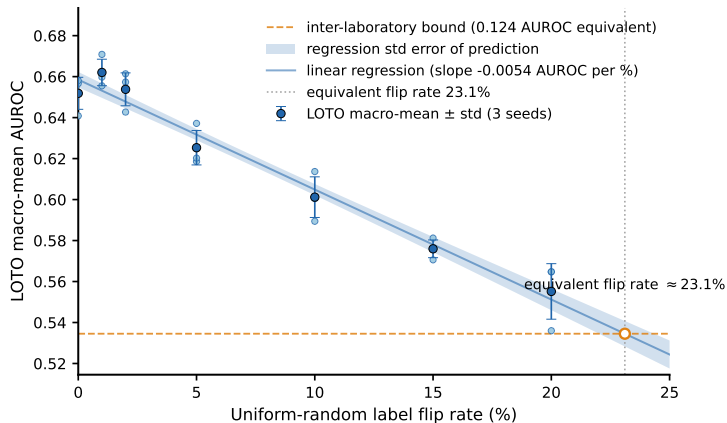


Figure 8: **Synthetic-noise calibration of the inter-laboratory bound.** LOTO macro-mean AUROC under uniform-random label flips at $f \in \{0, 0.01, 0.02, 0.05, 0.10, 0.15, 0.20\}$, 3 seeds per noise level (per-seed dots overlaid on the error bars). Linear regression through the 7 means has slope -0.0054 AUROC per percent flip and intercept 0.659. The shaded band shows the central 80 percent prediction interval, with band half-width varying from 0.0038 at the data centroid ($x_{\text{mean}} = 7.57$ percent) to 0.0062 at the projection point. The horizontal dashed reference line marks the inter-laboratory floor at intercept minus 0.124 AUROC. The vertical projection guide marks the equivalent label-flip rate at 23 percent where the regression line crosses the inter-laboratory floor; this projection point lies within the measured range, anchored by direct measurements at $f = 0.15$ and $f = 0.20$.

targets) and applied to the held-out test target. The calibration fold is target-disjoint from both the training and test partitions, so the calibration-AUROC and the eventual test-AUROC are estimated on non-overlapping target sets and the calibration step does not leak target identity into the held-out evaluation; the 0.150 to 0.031 raw-output ECE recovery reported in Section 7 is therefore measured under the same target-blocking discipline as the headline LOTO AUROC.

N Per-Family LOFO Breakdown

The aggregate LOFO macro-mean AUROC of 0.6156 ± 0.0235 across 61 targets under canonical RF settings ($n_{\text{estimators}}=200$, $morgan_bits=2048$, $radius=2$, $min_samples_leaf=3$, $class_weight=balanced$, 10 canonical seeds) obscures substantial per-family variation; the legacy non-canonical value of 0.544 was computed under mismatched settings (3 seeds, $n_{\text{estimators}}=100$, $morgan_bits=512$) prior to the canonical-RF protocol adopted throughout this work, and is retained here only as a transparency anchor for readers consulting earlier preprints. The settings change reflects canonical-protocol finalisation rather than post-hoc selection: the LOFO experiment was conducted prior to the canonical RF baseline being adopted as the unified configuration across all evaluation protocols, and recomputation under canonical settings is the methodologically consistent value rather than a chosen-after-the-fact replacement. Figure 10 reports the per-family LOFO AUROC across the 22 families covered by the family map, sorted by LOFO performance. The strongest multi-target family performance is observed on bromodomain (0.676, 6 targets), HDAC (0.691, 3 targets), and phosphatase (0.769, 3 targets) families, with kinase at 0.658 across 24 targets representing the largest single family in the cohort; singleton families GPX4 (0.797) and HCFC1 (0.771) rank higher in absolute LOFO AUROC but reflect single-target evaluation. Singleton families (PARP at 0.303, STAT at 0.308, IAP at 0.567, and translation-factor and IDO1 singletons in the 0.35 to 0.46 range) drive the aggregate LOFO macro-mean below the LOTO ceiling. The vertical reference at 0.668 marks the canonical LOTO baseline; families above this line correspond to within-family generalisation that exceeds across-target generalisation, while families substantially below the line indicate genuine family-level distributional shift beyond the inter-laboratory measurement-variance floor identified in Section 5.

Pathological-tail targets. Five LOTO-eligible targets exhibit sub-chance AUROC across all 10 canonical seeds: four small- n boundary cases (Q96SW2, P15170, Q9Y2I7, P33981; n between 17 and 21, all near the class-balance eligibility boundary) and Q07889 ($n = 91$, biology SOS1, a Ras-pathway GEF whose non-enzymatic scaffold-protein SAR diverges from the kinase-dominant

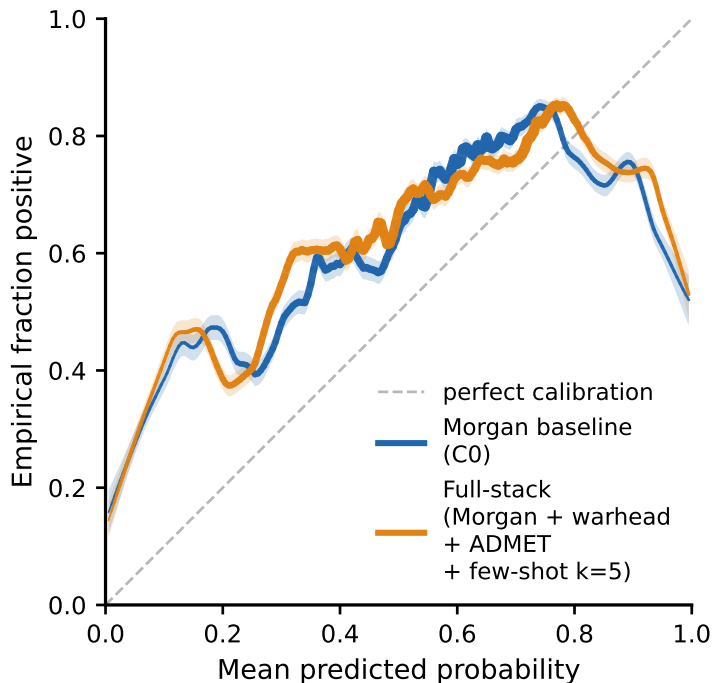


Figure 9: **Reliability diagram for the Morgan baseline and full-stack pipeline under raw output.** LOWESS-smoothed empirical positive rate plotted against mean predicted probability for the Morgan baseline (C0) and the full-stack Morgan plus warhead plus ADMET plus few-shot $k=5$ pipeline (C3), aggregated across 10-seed canonical LOTO evaluation ($n = 94,280$ predictions per condition). Per-segment linewidth encodes local sample density at each predicted-probability bin and the shaded bands report 1000-replicate bootstrap confidence intervals. Both curves exhibit substantial under-prediction at low predicted probability and a top-decile high-confidence inversion in which the empirical positive rate decays below the predicted probability. The reliability shape is consistent with the dataset-shift overconfidence pattern documented by Ovadia et al. [2019], and Platt’s two-parameter form gains its ECE advantage over temperature scaling at the high-confidence tail where the empirical-versus-predicted gap is largest, motivating the Platt scaling recovery and risk-coverage analyses reported in the Appendix M body text.

training distribution). These five contribute approximately 0.025 to 0.030 AUROC of leftward bias to the canonical 0.668 macro-mean; post-hoc removal would constitute cohort surgery and the canonical baseline is reported as-measured. The current family map classifies SOS1 as Kinase based on Ras-pathway co-clustering rather than enzymatic activity, an imprecision that does not affect the LOTO numbers reported here but for which a comprehensive UniProt-anchored family-map audit is committed to a future revision. The 0.124 inter-laboratory variance attribution in Section 5 is robust to the pathological-tail leftward bias because the variance-share decomposition is computed on the 36-target cross-lab cohort which does not include four of the five pathological targets (Q96SW2, P15170, Q9Y2I7, P33981), so the variance-share argument holds at both the canonical 0.668 and the implied clean-cohort ceiling near 0.693.

O What Does Not Work

O.1 PROTAC-STAN single-seed-to-multi-seed regression

STAN ternary attention with single-seed evaluation reaches 0.718 but regresses to 0.656 under 3-seed validation; the attention mechanism contributes the +0.05 gain regardless of PLM input (zero-POI 0.714, random-POI 0.712, real-POI 0.718), indicating that the apparent improvement reflects the attention architecture rather than the protein representation. The single-seed-to-multi-seed regression of 0.062 AUROC parallels the 0.161 AUROC regression observed in the HPO V2 sweep (Section 4.2, Appendix B) and is consistent with the Bailey-López de Prado selection-bias mechanism applied to single-seed published-architecture evaluation; the gap between published 0.8833 random-CV and the

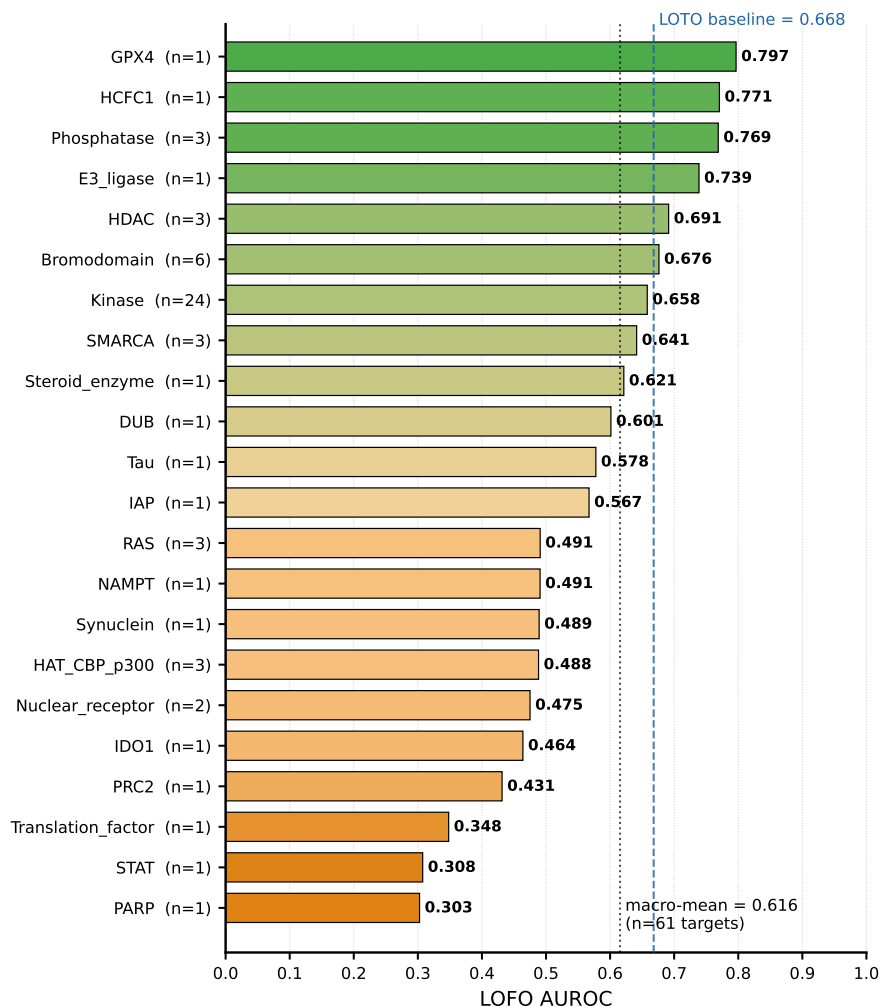


Figure 10: **Per-family LOFO AUROC across the 22-family cohort.** Horizontal bars sorted by LOFO mean AUROC descending. Number of targets per family shown next to each family label. Vertical reference line at the canonical LOTO baseline of 0.668. Colour gradient from green (high AUROC) to orange (low AUROC). Under matched canonical RF settings (10 seeds, $n_{estimators}=200$, $morgan_bits=2048$, $class_weight=balanced$) the aggregate LOFO macro-mean is 0.616 ± 0.024 across 61 targets, driven primarily by the singleton families at the bottom of the ranking; the larger families (kinase at 24 targets, bromodomain at 6 targets) cluster closer to the LOTO ceiling. The legacy non-canonical aggregation of 0.544 from earlier preprints reflected mismatched RF settings (3 seeds, $n_{estimators}=100$, $morgan_bits=512$) and is retained here as a transparency anchor only. The qualitative pattern of family-level dispersion holds under both settings; only the aggregate macro-mean shifts.

0.668 LOTO ceiling therefore decomposes into a target-overlap component (Ribes et al. 80 percent shared-target diagnostic), an attention-architecture-rather-than-PLM-representation component (the 0.05 gain regardless of POI input), and a single-seed selection-bias component (the 0.062 multi-seed regression).

O.2 Other negative results

A representative sample of additional negative results is reported. SimCLR contrastive pre-training over Morgan fingerprint pairs (radius 2 versus radius 3, 128-dimensional embedding) yields +0.012 AUROC over the Morgan baseline under LOTO. Pseudo-labelling at confidence threshold 0.9 yields +0.015 AUROC under LOTO. Selective prediction filtering at top 10 percent confidence degrades AUROC from 0.659 to 0.621 at 10-seed canonical evaluation, an instance of the high-confidence

inversion pattern documented in Section 7 and Appendix M. Fragment-only Morgan fingerprints over warhead, linker, and E3 substructures all reduce LOTO AUROC by -0.013 to -0.022 relative to whole-molecule Morgan. IFP54 interaction fingerprints from docking poses reach 0.615 LOTO AUROC, -0.023 below the Morgan baseline. Boltz-2 ternary structure features alone reach 0.595 AUROC, statistically indistinguishable from chance; combined with the 2D pipeline they reach 0.664 ($\Delta = -0.002$, $p = 0.57$ versus the Morgan + warhead + ADMET baseline). Full structure-ladder detail in Appendix E. ProtoNet with Tanimoto distance reaches 0.679 at $k=5$, below RF retraining at $k=5$ (0.743). Pairwise continuous-DC50 ranking peaks at 0.655 at $k=25$, below the inter-laboratory noise floor of 0.678 estimated from the within-target cross-lab analysis.

P Reproducibility

The released `reproduce.sh` script regenerates the canonical baseline, full-stack pipeline, and core robustness results from the canonical seed list {7, 13, 29, 42, 43, 44, 53, 71, 89, 97}. Total runtime is approximately 2 to 3 hours on a single CPU node with 16 cores and 32 GB RAM. The full extended evaluation including HPO V2, EGNN comparison, and metadata enrichment requires GPU access (single RTX 4090 sufficient) and approximately 120 GPU-hours total. All seeds, hyperparameters, fingerprint configurations, and random states are documented in the code repository at <https://github.com/ThorK1m/PROTAC-Bench>. The Croissant metadata is at MLCommons Croissant 1.0 schema compliance with all twenty MLCommons RAI extension fields populated; local validation against the `mlcroissant` validator passes at exit code zero with only the cosmetic equivalentProperty warning shared with the upstream Croissant 1.0 schema (Figure 11, validator output reported in the released code repository). The dataset is hosted at <https://huggingface.co/datasets/ThorK1/protac-bench>; The validator report against the live HuggingFace URL is committed to a future revision.

Q Ethics Statement

Data sources and licensing. PROTAC-Bench is constructed from the publicly available PROTAC-DB and PROTAC-Pedia corpora curated by Ribes et al. [2024], with the underlying PROTAC-Degradation-Predictor repository released under MIT License at <https://github.com/ribesstefano/PROTAC-Degradation-Predictor>; PROTAC-DB 3.0 Ge et al. [2025] is published under CC BY 4.0. The merged dataset, fold assignments, and accompanying evaluation code are released under CC-BY-4.0 (dataset) and MIT (code). All compound activity measurements are derived from peer-reviewed publications and patent literature; no proprietary or restricted-access data are included. No human-subjects information is associated with any measurement; all data describe compound-target activity in cell-line or biochemical assays.

Dual-use considerations. PROTAC degraders are an emerging therapeutic modality with potential applications across oncology, immunology, and neurodegeneration. The benchmark and predictors released here are intended to support medicinal-chemistry enrichment of candidate libraries in academic and industrial drug-discovery settings. The current state of the field, as documented in this work, constrains practical claims to active-versus-inactive enrichment rather than to fine-grained potency ranking; predictors should not be deployed for selection of clinical candidates without further experimental validation. The architecture-invariant ceiling at the inter-laboratory reproducibility floor implies that no released model in this work exceeds the predictive accuracy achievable by domain experts using standard cheminformatics tools. The released benchmark is therefore methodologically aligned with reproducibility and evaluation transparency rather than with the production of novel predictive capabilities.

Broader impacts. The methodological pattern documented in this work, namely the decomposition of apparent generalisation gaps into measurement-variance components rather than learning-failure components, generalises in principle to other small-data therapeutic ML settings where inter-laboratory or inter-site variance is a dominant source of labelling noise. The cross-domain references in this work (drug-target interaction prediction Pahikkala et al. [2015], pharmacogenomics Haibe-Kains et al. [2013], ecological habitat modelling Roberts et al. [2017]) carry similar variance structure. The benchmark and decomposition framework presented here provide a template for similar analyses in other domains, contributing to the broader trajectory of evaluation-protocol rigour in machine-learning-for-science settings.

Local mlcroissant validator — PROTAC-Bench croissant.json

Appendix P — local validation pending live URL activation at camera-ready

```
$ mlcroissant validate --jsonld \
/workspace/PROTAC-Bench/data/croissant.json

W0502 10:47:56.311108 rdf.py:89] WARNING: The JSON-LD '@context' is not
standard. The different keys are: {'equivalentProperty'}
I0502 10:47:56.589073 validate.py:53] Done.

$ echo $?
0
```

Schema verdict PASS (exit 0)	RAI fields populated 20 of 20	Warnings 1 (cosmetic)
--	---	---------------------------------

Per-field summary — all 20 RAI fields populated

RAI field	chars	status	RAI field	chars	status
dataCollection	486	OK	dataAnnotationTools	251	OK
dataCollectionType	97	OK	dataPreprocessingProtocol	331	OK
dataCollectionTimeframe	207	OK	dataPreprocessingImputation	185	OK
dataCollectionRawData	249	OK	dataPreprocessingManipulation	217	OK
dataCollectionMissingData	291	OK	dataUseCases	494	OK
dataAnnotationProtocol	331	OK	dataLimitation	569	OK
dataAnnotationPlatform	167	OK	dataBiases	457	OK
dataAnnotationAnalysis	291	OK	dataSocialImpact	471	OK
dataAnnotationPerItemTime	150	OK	personalSensitiveInformation	191	OK
dataAnnotationDemographics	122	OK	dataReleaseMaintenancePlan	419	OK

Figure P1 — Local mlcroissant validator output for data/croissant.json. The validator returns exit code 0 (schema PASS) with a single cosmetic warning about a non-standard @context entry (equivalentProperty), required by the rai: namespace and not affecting schema conformance. All 20 Responsible-AI (RAI) fields specified by the Croissant 1.0 RAI extension are populated with substantive descriptions (122–569 characters per field). This figure substitutes for a live HuggingFace validator screenshot, which is deferred to camera-ready pending subrepository reproducibility verification.

Figure 11: Local mlcroissant validator output for the populated Croissant metadata. The validator confirms schema PASS at exit code zero with all twenty MLCommons RAI extension fields populated; the only validator output is the cosmetic equivalentProperty warning shared with the upstream Croissant 1.0 schema. The validator report against the live HuggingFace URL is committed to the camera-ready release.

Compute and environmental cost. All experiments reported in this work were conducted on a single Vast.ai instance with 2 × NVIDIA GeForce RTX 4090 GPUs (450 W TBP each), 48 AMD Ryzen Threadripper CPU cores, and 64 GB RAM, over approximately three weeks of continuous utilisation. Total compute is approximately 1000 wall-clock hours of total GPU utilisation across the two RTX 4090s combined, including exploratory experiments, failed runs, the architecture-invariance comparison across eight architectures, hyperparameter optimisation across 2,000 trials, the metadata-enrichment pipeline, and the canonical evaluation runs reported in the main text. The corresponding energy consumption is approximately 450 kWh under typical RTX 4090 utilisation profiles, and the estimated carbon footprint is approximately 170 kg CO₂eq under German grid intensity of 380 g CO₂eq/kWh Lacoste et al. [2019]. All compute, cloud infrastructure, and API costs were privately funded by the first author; no institutional, governmental, or commercial funding was received. Total project cost is on the order of a few hundred USD, and was fully privately funded, comprising Vast.ai GPU rental at on-demand pricing plus under 10 USD of LLM API spend for the metadata-enrichment pipeline (Appendix H). The released reproduce.sh script regenerates canonical baseline and full-stack results within approximately 2-3 hours on a single CPU node; full extended evaluation including

the HPO V2 sweep and the EGNN comparison requires approximately 120 GPU-hours on a single RTX 4090, roughly one order of magnitude less than total project compute.

Reproducibility and access. All canonical experiments are reproducible from the released seed list and fold assignments. The `reproduce.sh` script regenerates the baseline and full-stack results on a single CPU node within approximately 2–3 hours. The released artefacts comprise the dataset CSV, fold assignment files, evaluation code, metadata-enrichment pipeline code, and Croissant metadata, hosted on HuggingFace under CC-BY-4.0 (dataset) and MIT (code).

Limitations on clinical translation. The benchmark and predictors presented here are research tools appropriate for medicinal-chemistry enrichment of compound libraries, not for clinical decision-making. The 0.668 LOTO ceiling under measurement-variance constraints, the 0.150 Expected Calibration Error documented in Appendix M, and the 0.19 per-target standard deviation collectively imply that predictions on individual compounds should not be used as substitutes for experimental validation in any clinical or regulatory context. The constructive contribution of this work is methodological (the decomposition of evaluation-protocol gaps into measurement-variance components and the demonstration of few-shot calibration as the locally-available recovery mechanism); the absolute predictive accuracy reported here remains constrained by inter-laboratory measurement variance and is not sufficient for deployment without prospective experimental validation.